UNIVERSITE DE LIEGE

Faculté des Sciences

First-principles study of ferroelectric oxides: dynamical properties & electron localization tensor

Veithen Marek

Promoteur:
Prof. Ph. Ghosez

Membres du jury:
Prof. X. Gonze
Prof. Y. Lion

Juin 2003

Contents

Introduction

Ferroelectric oxides are insulating solids characterized, in a given temperature range, by a switchable spontaneous polarization [1]. At high temperatures, they are in a high-symmetry paraelectric phase. As the temperature is lowered, they undergo one or several transitions to ferroelectric phases characterized by a lower symmetry. These materials are of great importance for numerous applications. Their multistability allows the realization of nonvolatile ferroelectric memories [2, 3]. Furthermore, ferroelectric materials usually combine very large dielectric, piezoelectric, pyroelectric, non-linear optic and electrooptic responses. The piezoelectric effect is exploited in transducers and actuators [4, 5], designed to convert an electrical signal into a mechanical one, or vice versa. Because of their large electrooptic and non-linear optical coefficients, ferroelectric materials are also widely used in telecommunications [6, 7], holography [8, 9] or for the frequency doubling of lasers.

Nowadays, many physical properties of solids and molecules can be calculated and predicted very accurately from first-principles, taking as only inputs the atomic numbers of the constituent atoms. One of the most powerful techniques available is the Kohn-Sham density functional theory [10, 11]. Combined with linear response techniques this method has already played an important role to elucidate the physics of ferroelectric oxides [12]. Its systematic application to a large number of compounds improved our understanding of their structural, electronic, dielectric and piezoelectric properties. Unfortunately, there has been no similar study of related quantities such as the electron localization tensor. Moreover, most first-principles studies have been performed on perovskite ferroelectrics such as barium titanate ($BaTiO_3$) or lead titanate ($PbTiO_3$) and only little attention has been paied to compounds with a trigonal structure such as lithium niobate ($LiNbO_3$). These two points will be adressed in this work.

In the first chapter we investigate the linear dielectric and dynamical properties of lithium niobate ($LiNbO_3$). This material is known to have exellent electrooptic and non-linear optical properties. It is widely used in various fields including telecommunications and holography. In order to understand the origin of its exellent coupling coefficients, it is essential to have a detailled understanding of the linear dielectric and dynamical properties of this compound.

In the first chapter, we investigate the problems related to the assignation of the phonon modes in the ferroelectric phase, the origin of the anomalous effective charges and the mechanisme of the structural phase transition. In particular, we report fundamental quantities that have never been computed before in this compound such as the Born effective charges, the spontaneous polarization or the static and optical dielectric tensors.

The second chapter is devoted to a topic related with the modern theory of polarization [13, 14, 15]. In extended systems, the electric field perturbation requires a careful treatment. Crystalline solids are usually described using periodic Born von Karman boundary conditions. These boundary conditions are incompatible with the scalar potential $\boldsymbol{\mathcal{E}} \cdot \mathbf{r}$ that enters the Kohn-Sham Hamiltonian since the position operator $\boldsymbol{r}$ breaks the periodicity of the crystal lattice. Nevertheless, thanks to the modern theory of polarization it is possible to study the linear and non-linear response of a periodic solid to an electric field. Moreover, we are able to adress more fundamental questions such as the problem of electron localization. In the second chapter we study the electron localization tensor in various oxides including the ferroelectric perovskites $BaTiO_3$ and $PbTiO_3$. Similar studies on zincblende semiconductors [16] and IV-VI chalcogenides [17] have shown that this concept can give useful informations about the electronic properties of a compound when it is systematically applied to a family of solids with related structures.

We first set up a band-by-band decomposition of the localization tensor. In the first chapter, such a decomposition has already revealed to be useful to relate the anomalous Born effective charges in $LiNbO_3$ to the particular electronic structure of this compound. In case of the localization tensor, it gives an even deeper insight in the kind of hybridizations that take place in a solid. In particular, we investigate the variations of electron localization during the ferroelectric phase transtion of $BaTiO_3$. We show that the results are consitent with the electronic structure as it is interpreted in the Harrison model.

Chapter 1

First-principles study of lithium niobate

Using a first-principles approach based on density functional theory, the electronic, dielectric and dynamical properties of the two phases of lithium niobate are studied. In particular, the spontaneous polarization, the optical dielectric tensors, the Born effective charges and the zone-center phonons are computed. The Born effective charges are found to be significantly larger than the nominal ionic charges of the ions, a feature similar to what is observed in related ABO_3 compounds and attributed to the hybridization between the O 2p and Nb 4d states. The analysis of the zone-center phonons in the paraelectric phase reveals an unstable A_{2u} mode to be responsible for the phase transition. The origin of the structural instability is attributed to destabilizing long-range dipolar interactions which are not fully compensated by stabilizing short-range forces. Finally, the identification of the E modes in the ferroelectric phase, that is still cause for debates in spite of the numerous experimental and theoretical studies, is discussed and a new assignation based on the analysis of the mode oscillator strengths and of the angular dispersion relation of extraordinary phonons is proposed.

1.1 Introduction

Lithium niobate ($LiNbO_3$) belongs to the class of ferroelectric oxydes. Its good electro-optic, photorefractive and non-linear optical properties make it nowadays a widely used material in devices like modulators for fiber-optic communications systems [1, 6, 7] or holographic applications [8, 9].

Many ABO_3 coumpounds like $BaTiO_3$ have a perovskite structure [1]. In contrast, lithium niobate has two phases of trigonal symmetry with 10 atoms per unit cell: a high symmetric paraelectric phase (space group $R\overline{3}c$) stable above 1480 K, and a ferroelectric ground state (space group R3c). Because of its high transition temperature T_c and due to the fact that its melting point (about 1520 K) is quite close to T_c, only few experimental data are available on the paraelectric phase. On the contrary, during the last decades, the ferroelectric phase has been the subject of numerous experimental and theoretical studies.

A good review, that summarizes a wide range of experimental results is proposed in Ref. [21]. From a theoretical point of view, a few first-principles studies have been performed. Without being exhaustive, let us cite the papers of Inbar and Cohen [22, 23] who identified the nature of the phase transition to be mainly of the order-disorder type. More recently, Caciuc, Postnikov and Borstel [24, 25] have calculated zone-center phonons in the ferroelectric phase, and Parlinski, Li and Kawawzoe [26] have obtained phonon dispersion relations in the two phases.

The present work is intended to complete the set of existing data on lithium niobate. In particular, we report the Born effective charges and the optical dielectric tensors in the two phases. The knowledge of these quantities allows us to deduce the frequencies of the longitudinal phonon modes at the Γ-point and to investigate the origin of the ferroelectric instability. We also pay a particular attention to the assignation of the E phonon modes in the ferroelectric phase. We draw several comparisons with the perovskites and we show that, in spite of its different structure, $LiNbO_3$ has a very similar behaviour. Beside using the local density approximation (LDA), as it was the case in the previous works cited above, we also compute some properties within a generalized gradient approximation (GGA) for the exchange-correlation energy. This allows to compare the results and to examine the impact of both kinds of approximations.

This chapter is organized as follows. Using a first-principles density functional approach, we first study ground-state properties (section 1.3) like the atomic and electronic structures and the spontaneous polarisation appearing during the phase transition. We then discuss dielectric properties (section 1.4) like the optical dielectric tensor and the Born effective charges. We finally report the phonons at the Γ-point (section 1.5) in the two phases and deduce the static dielectric tensor for the ferroelectric phase.

1.2 Method

Our calculations were performed in the framework of the density functional theory (DFT) as it was developed by Hohenberg, Kohn and Sham [10, 11]. We used the ABINIT [27] package, a planewave pseudopotential DFT code.

For the exchange-correlation functional, we chose either the local density approximation (LDA) as parametrized by Perdew and Wang [33] or the generalized gradient approximation (GGA) proposed by Perdew, Burke and Erzenhof [34]. The all-electron potentials were replaced by norm-conserving pseudopotentials generated according to the Troullier-Martins scheme [35] thanks to a package developed at the Fritz-Haber Institute, Berlin [36]. Niobium 4s, 4p, 4d and 5s electrons, lithium 1s and 2s electrons as well as oxygen 2s, 2p electrons were considered as valence states in the construction of the pseudopotentials.

For the calculations within the LDA, the wave functions were expanded in plane waves up to a kinetic-energy cutoff of 45 Ha and the Brillouin zone was sampled using a $6 \times 6 \times 6$ Monkhorst-Pack [37] mesh of special k-points. These parameters were necessary to obtain converged results in the linear-response calculations of phonon frequencies and Born effective charges. A 35 Ha cutoff and a $4 \times 4 \times 4$ grid of special k-points were already enough to obtain converged values for the lattice constants and atomic positions and were used in the GGA determination of these quantities.

1.3 Ground-state properties

1.3.1 Structural data

As a first step, we determined the structural parameters of lithium niobate in its two phases by relaxing simultaneously the cell shape and the atomic positions. In the optimized structures reported here, the forces on the atoms are less than 10^{-5} hartree/bohr and the stresses on the unit cell are smaller than 10^{-7} hartree/bohr^3. The two phases of $LiNbO_3$ are rhombohedral with 10 atoms in the unit cell. To describe their geometry, one can either use the primitive (rhombohedral) or an hexagonal unit cell. In the discussion of our results, the symbols a and c correspond to the lengths of the basis vectors of the hexagonal unit cell. Atomic positions are given in hexagonal coordinates.

The paraelectric phase belongs to the space group R$\overline{3}$c. The positions of the 10 atoms in the rhombohedral unit cell are shown on Figure 1.1. The threefold axis is formed by a chain of equidistant niobium and lithium atoms. Each niobium is located at the center of an octaedron formed by 6 oxygen atoms. In Table 1.1, we define the parameters that determine the atomic positions in the two phases by reporting the hexagonal coordinates of five atoms of the rhombohedral unit cell. The coordinates of the other atoms can easily be obtained by using the symmetry operations of the space groups R$\overline{3}$c and R3c.

In the paraelectric phase, the positions of the niobium and lithium atoms are fixed by symmetry while the positions of the oxygen atoms are determined by the internal parameter x. The results of our structural optimizations are summarized in Table 1.2. They are compared to the results obtained by Parlinski *et al.* [26] and Caciuc *et al.* [24] as well as to the experimental data deduced from neutron diffraction on a powder [38]. The GGA gives the closest agreement with the experiment whereas our LDA results present errors similar to those of the previous DFT calculations (also performed within the LDA).

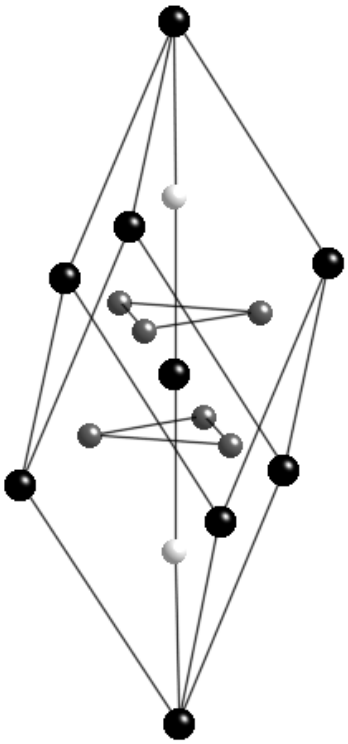

Figure 1.1: Primitive unit cell of the paraelectric phase of $LiNbO_3$.

The ferroelectric phase belongs to the space group R3c. During the structural optimizations, we held the niobium Nb_1 atom fixed at the origin. The coordinates of the lithium and oxygen atoms are reported in the lower part of Table 1.1. Our results for the ferroelectric phase are summarized on Table 1.3. As for the paraelectric phase, our values are close to those of Parlinski *et al.* [26]. Again, we tried to improve the accuracy of the calculation using the GGA. However, this does not yield a significative improvement: looking for example at the value of the parameter a, we observe that the GGA tends to overcorrect the errors of the LDA, a fact already observed in this kind of calculations [39, 40].

Comparing Table 1.2 and 1.3, we see that our values for the lattice parameters are in better agreement with the experiment for the ferroelectric than for the paraelectric phase. A possible explanation is that we determined the ground-state of the compound at 0 K and we thus neglected the effects of the thermal expansion. As the paraelectric phase of lithium niobate is only stable above 1480 K, these effects are more important for this phase than for the ferroelectric one and the calculated parameters tend to be smaller than the measured ones.

Phase	Atom	Position		
Paraelectric	Nb_1	$(\ 0,$	$0,$	$0\ )$
	Li_1	$(\ 0,$	$0,$	$\frac{1}{4}\ )$
	O_1	$(\ -\frac{1}{3},$	$-\frac{1}{3}+x,$	$\frac{7}{12}\ )$
	O_2	$(\ \frac{1}{3}-x,$	$-x,$	$\frac{7}{12}\ )$
	O_3	$(\ x,$	$\frac{1}{3},$	$\frac{7}{12}\ )$
Ferroelectric	Nb_1	$(\ 0,$	$0,$	$0\ )$
	Li_1	$(\ 0,$	$0,$	$\frac{1}{4}+z\ )$
	O_1	$(\ -\frac{1}{3}-u,$	$-\frac{1}{3}+v,$	$\frac{7}{12}-w\ )$
	O_2	$(\ \frac{1}{3}-v,$	$-u-v,$	$\frac{7}{12}-w\ )$
	O_3	$(\ u+v,$	$\frac{1}{3}+u,$	$\frac{7}{12}-w\ )$

Table 1.1: Atomic positions (in hexagonal coordinates) in the two phases of litihium niobate.

	a(Å)	c(Å)	x
Exp. [38]	5.289	13.848	0.060
Calc. (LDA) [24]	5.138	13.499	0.049
Calc. (LDA) [26]	5.097	13.708	0.036
Present (LDA)	5.125	13.548	0.042
Present (GGA)	5.255	13.791	0.048

Table 1.2: Lattice constants and atomic position parameter x (see Table 1.1) in the paraelectric phase of lithium niobate.

1.3.2 Electronic properties

In Figure 1.2, we report the Kohn-Sham band structure of the paraelectric phase of lithium niobate. The notations of the high symmetry points between which we have drawn the band structure correspond to those chosen in Ref. [41]. We observe the presence of well separated groups of bands. Each of these groups has a marked dominant character and has been labeled by the name of the atomic orbital that mainly composes this energy state in the solid.

As previously discussed by Inbar and Cohen [22, 23], the chemical bonding in lithium niobate has a mixed covalent-ionic character. The Nb 4d and O 2p atomic orbitals strongly interact to form the valence and conduction bands near the Fermi level while the Li atoms completely loose their 2s electrons. In other words, the bonding between niobium and oxygen atoms has a non-negligible covalent character while the bonding with the lithium atoms is essentially ionic. This mixed feature is similar to what has been observed in most perovskite ABO_3 compounds like $KNbO_3$ and $BaTiO_3$ [42] but different from the case of $PbTiO_3$ [43, 44, 45], in which the lead atom has a covalent interaction with the oxygen.

In Figure 1.3, we compare the Kohn-Sham electronic band structure of the two phases

	a(Å)	c(Å)	z	u	v	w
Exp. [38]	5.151	13.876	0.0329	0.00947	0.0383	0.0192
Calc. (LDA) [26]	5.086	13.723	0.0350	0.01497	0.0247	0.0186
Present (LDA)	5.067	13.721	0.0337	0.01250	0.0302	0.0183
Present (GGA)	5.200	13.873	0.0318	0.00973	0.0382	0.0199

Table 1.3: Lattice constants and atomic position parameters (see notations of Table 1.1) in the ferroelectric phase of lithium niobate.

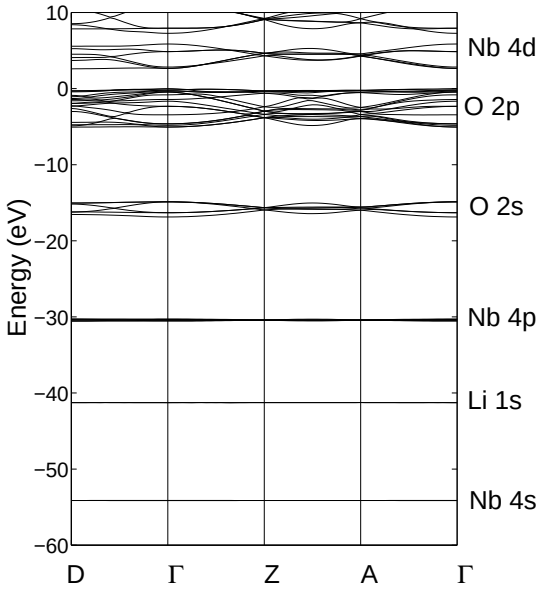

Figure 1.2: Kohn-Sham electronic band structure in the paraelectric phase of $LiNbO_3$ calculated within the LDA.

of $LiNbO_3$ in the region close to the fermi level. The transition to the ferroelectric state is accompanied by a strong increase of the indirect bandgap E_g from 2.60 to 3.48 eV and a reduction of the spread of the O 2p bands from 5.06 to 4.71 eV. We note that, in spite of the well known DFT bandgap problem [46], the value of the E_g in the ferroelectric phase only slightly underestimates the experimental value of 3.78 eV [47]. For the deeper bands not mentioned on the picture, we observed that the spread remains unaffected at the transition while the position with respect to the top of the valence band is slightly shifted to higher energies. We conclude that the only significant effect of the phase transition on the electronic properties is to modify the hybridizations between O 2p and Nb 4d orbitals.

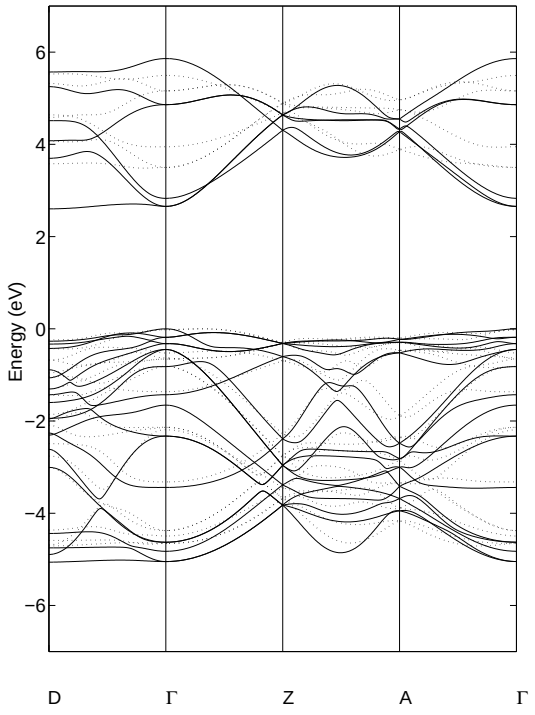

Figure 1.3: Kohn-Sham electronic band structure near the Fermi level in the paraelectric (solid line) and ferroelectric (dashed line) phases of $LiNbO_3$ calculated whitin the LDA.

1.3.3 Spontaneous Polarization

The modern theory of polarization, as it was developped by R. Resta [13], R. D. King-Smith and D. Vanderbilt [14, 15], identifies the spontaneous polarization of a ferroelectric material to a Zak-phase of the electronic wavefuntions. We used this approach to calculate the spontaneous polarization of lithium niobate.

The formulas we used are described in Ref. [14] (in particular equation (16)). To calculate the polarization, we sampled the Brillouin zone by a $4 \times 4 \times 20$ mesh of k-points. We calculated the polarization for the two phases of $LiNbO_3$ and then took the difference to get the spontaneous polarization. Our results, obtained in LDA and GGA, are summarized in Table 1.4. We compare them to experimental values obtained by a field reversal method [48] and a pyroelectric measurement [49]. For completeness, we also mention a value reported by Hafid *et al.* [50] even if their calculation was conceptually wrong in the sense that it was making use of static charges deduced from a population analysis of the Xα electronic distribution of a NbO_6 cluster, instead of the dynamical Born effective charges (see Section 1.4.2).

	P_s (C/m^2)
exp. [48]	0.71
exp. [49]	0.70
calc. [50]	0.77
LDA	0.80
GGA	0.80

Table 1.4: Spontaneous polarization of lithium niobate.

Our values overestimate the experimental results by 0.1 C/m^2. This agreement is not perfect but comparable to what has been obtained in perovskite ferroelectrics [51]. Part of the error could be assigned to the use of DFT and approximate functionals [52]. Another origin for the error could be attributed to the fact that our calculated value is an upper limit, related to an idealized perfect crystal. A real sample always presents defects that tend to lower the measured polarization.

1.4 Dielectric properties

1.4.1 The optical dielectric tensor

We have calculated the optical dielectric permitivity tensors, $\varepsilon^{\infty}_{\alpha\beta}$, in the two phases of lithium niobate. This tensor is related to a second derivative of the electronic energy with respect to an electric field and has been computed using a linear response technique [31]. All calculations were done using the LDA and no scissors correction has been included. Our results are summarized in Table 1.5, where we also compare the values in the ferroelectric phase to the experiment. The tensors are reported in cartesian coordinates with

the z axis along the ferroelectric direction (vector c of the hexagonal unit cell, see section 1.3.1), the y axis in a gliding plane perpendicular to an a axis and x along a.

Phase		reference	$\varepsilon^{\infty}_{xx}$	$\varepsilon^{\infty}_{yy}$	$\varepsilon^{\infty}_{zz}$
Paraelectric	calc.	present	6.1	6.1	6.9
Ferroelectric	calc.	present	5.6	5.6	5.5
	exp.	[[65]]	5.0	5.0	4.6

Table 1.5: Optical dielectric tensors (in cartesian coordinates) in the two phases of lithium niobate.

The calculated values overestimate the experimental results [53]. This problem has been previously discussed in the litterature [54, 55] and has been related to the lack of polarization dependence of local and quasi-local exchange-correlation functionals (LDA, GGA). In spite of this error on the absolute value, the evolutions of ε^{∞} are in general qualitatively well described by LDA calculations.

We first notice that, as observed in related ABO_3 perovskite compounds like $BaTiO_3$ [56] and $KNbO_3$ [57], the amplitude of the dielectric tensor decreases at the transition from the paraelectric to the ferroelectric phase. This can be correlated with the evolution of the bandgap. Also, the lowering is strongest along the ferroelectric z direction so that the nature of $LiNbO_3$ changes at the transition from positively uniaxial ($\varepsilon^{\infty}_{zz}/\varepsilon^{\infty}_{xx} > 1$) to negatively uniaxial ($\varepsilon^{\infty}_{zz}/\varepsilon^{\infty}_{xx} < 1$). Another interesting comparison with perovskite compounds concerns the absolute value of ε^{∞}. The amplitude of $\varepsilon^{\infty}_{zz}$ in $LiNbO_3$ is close to what is reported for the cubic and rhombohedral phases of $KNbO_3$ [57] (6.63 and 5.49 respectively) while the elements $\varepsilon^{\infty}_{xx}$ and $\varepsilon^{\infty}_{xx}$ are slightly smaller (6.63 and 5.93 repectively in $KNbO_3$).

1.4.2 Born effective charges

The Born effective charges (Z^*) play a fundamental role in the dynamics of insulating crystal lattices. They govern the amplitude of the long-range Coulomb interaction between nuclei and the splitting between longitudinal (LO) and transverse (TO) optic phonon modes. The Born effective charge tensor of an atom κ is defined as the coefficient of proportionality, at the linear order and under the condition of zero macroscopic electric field, between the macroscopic polarization per unit cell created in the direction β and a cooperative displacement of atoms κ in the direction α

$$Z^*_{\kappa,\alpha\beta} = \Omega_0 \frac{\partial P_\beta}{\partial \tau_{\kappa,\alpha}}\bigg|_{\mathcal{E}=0} \tag{1.1}$$

where Ω_0 is the unit cell volume. As previously discussed in the litterature (see for instance Ref. [58]), Z^* is a dynamical quantity, strongly influenced by dynamical changes of orbital hybridization induced by the atomic displacements. As a consequence, its amplitude is not direclty related to that of the static charges and can take anomalous values.

We calculated the Born effective charge tensors in the two phases of $LiNbO_3$ using both the linear response formalism (LDA calculation) and the Berry phase approach (LDA + GGA calculations). Table 1.6 summarizes the results obtained by linear response for Li_1, Nb_1 and the three O_1, O_2, O_3 oxygen atoms. At the last line, we mention the eigenvalues of the symmetric part of Z_O^* that are identical for all the oxygens. The labels of the atoms correspond to those defined in section 1.3.1. The tensors are reported in cartesian coordinates using the same set of axis as for the dielectric tensor (section 1.4.1).

	paraelectric phase			ferroelectric phase		
Li_1	1.15	0	0	1.19	-0.25	0
	0	1.15	0	0.25	1.19	0
	0	0	1.11	0	0	1.02
Nb_1	8.28	2.07	0	7.32	1.65	0
	-2.07	8.28	0	-1.65	7.32	0
	0	0	9.17	0	0	6.94
O_1	-1.80	0	0	-1.62	0.31	-0.17
	0	-4.48	2.46	0.23	-4.06	1.79
	0	2.32	-3.43	-0.13	1.85	-2.66
O_2	-3.81	-1.16	-2.13	-3.22	-1.15	-1.46
	-1.16	-2.47	-1.23	-1.23	-2.46	-1.04
	-2.01	-1.16	-3.43	-1.53	-1.04	-2.66
O_3	-3.81	1.16	2.13	-3.68	0.96	1.63
	1.16	-2.47	-1.23	0.88	-2.00	-0.75
	2.01	-1.16	-3.43	1.67	-0.81	-2.66
O (eig.)	-6.40	-1.51	-1.80	-5.33	-1.41	-1.60

Table 1.6: Born effective charges (in atomic units) of Nb_1, Li_1, O_1, O_2 and O_3 in the two phases of lithium niobate. The last line gives the eigenvalues of the symmetric part of Z_O^* (identical for all the oxygens).

For comparison, we also determined Z_{Nb}^* using the so called "Berry phase approach", by approximating Eq. (1.1) by a finite difference expression :

$$Z^*_{\kappa,\alpha\beta} \simeq \Omega_0 \frac{\Delta P_\beta}{\Delta \tau_{\kappa,\alpha}}. \tag{1.2}$$

in which the electronic contribution to the change of polarization is estimated using the same approach as in Section 1.3.3. To calculate Z_{Nb}^*, we displaced the niobium atom

by 0.02 Bohr along the three primitive vectors of reciprocal space and we calculated the polarization difference between this configuration and the equilibrum configuration along these three directions. As in section 1.3.3, we used a grid of 20 k-points in the direction along with we calculated the polarization and 4 k-points in the two other directions. We finally performed a transformation to get the cartesian components of these tensors. LDA and GGA results are summarized on Table 1.7.

	paraelectric phase			ferroelectric phase		
LDA	8.26	2.07	0	7.30	1.61	0
	-2.07	8.26	0	-1.61	7.30	0
	0	0	9.08	0	0	6.83
GGA	8.40	2.10	0	7.23	1.59	0
	-2.10	8.40	0	-1.59	7.23	0
	0	0	9.29	0	0	6.46

Table 1.7: Born effective charges of the niobium atom calculated using the Berry phase approach in LDA and GGA.

As expected, within the LDA, the tensors obtained by linear response or using the Berry phase approach are identical within the accuracy of the calculation (± 0.02). However, we note that we had to use a plane-wave kinetic energy cutoff of 45 hartree to get converged results by linear response whereas a smaller value of 35 hartree was sufficient using the Berry phase approach. We also observe differences between LDA and GGA results, the largest one being for the $Z^*_{Nb,33}$ element. In order to get a better insight on the influence of the exchange-correlation functional, we recomputed Z^*_{Nb} in the paraelectric phase using the GGA wavefunctions but with the geometric parameters (atomic positions and lattice constants) obtained in LDA:

$$Z^*_{Nb} = \begin{pmatrix} 8.30 & 2.08 & 0 \\ -2.08 & 8.30 & 0 \\ 0 & 0 & 9.12 \end{pmatrix}. \tag{1.3}$$

We observe that the tensor in now very close to the one obtained in LDA. The difference between the results reported in Table 1.7 comes therefore principally from the fact that LDA and GGA give slightly different geometrical parameters whereas the Berry phase itself is quite insensitive to the approximation used for the exchange-correlation energy.

Analysing now the charges reported in Table 1.6, we observe that Z^*_{Li} is nearly isotropic and that the diagonal elements have a value close to the nominal charge of the lithium atom (+1). At the opposite, the amplitude of Z^*_{Nb} is highly *anomalous* in the sense that it is significantly larger than the nominal charge expected in a purely ionic crystal (+5). The niobium charge is slightly anisotropic with a significantly different value along the trigonal axis. For the oxygen atoms, the anisotropy is much stronger. This feature appears

clearly form the inspection of the tensor eigenvalues. The highest eigenvalue is strongly *anomalous* (-6.4 for the paraelectric phase, to be compare to the nominal charge of -2) and the inspection of the associated eigenvector reveals that it is the charge associated to an oxygen displacement (nearly) along the Nb–O bond. In contrast, the two other eigenvalues (associated to oxygen displacement in the plane perpendicular to the Nb–O bond) are smaller than -2.

Most of our observations on $LiNbO_3$ are comparable to what has been previously reported for related perovskite compounds like $KNbO_3$ [57, 51] or $NaNbO_3$ [51]. For instance, the Nb charge in the paraelectric phase for a displacement along the Nb–O bond is respectively equal to 8.75, 9.11 and 9.23 in $LiNbO_3$, $NaNbO_3$ [51] and $KNbO_3$ [51] while the Li, Na and K charge are equal respectively to 1.11, 1.13 and 1.14.

The amplitude of the charge in $LiNbO_3$ can be explained following the same line of thought than Ghosez *et al.* for perovskite compounds in Ref. [58] . The Li atom is close to a fully ionized configuration and only carries its nominal charge. At the opposite, there is a partly covalent interaction between Nb and O which is responsible for their *anomalous* effective charges and for the strong anisotropy of the oxygen tensor, as it is made plausible within the bond orbital model of Harisson [59]. During an atomic displacement, the parameters that determine the covalent interactions between the Nb 4d and O 2p atomic orbitals (the hopping integrals) vary. This variation produces a dynamical charge transfer between the niobium and the oxygen atoms which is at the origin of the anomalous part of Z^*_{Nb} and Z^*_O.

The essential role played by the O 2p bands can be emphasized from the analysis of the contribution of the different isolated sets of bands (as identified in Figure 1.2) to the global niobium charge. Individual contributions were obtained thanks to formula (16) of Ref. [14] by considering only the Bloch functions associated to a particular set of bands as elements of the overlap matrix. The results of the decomposition are summarized in Table 1.8. The first line (Z_{core}) brings together the nucleus and core electrons contributions. The last line corresponds to the total charge. The second column refers to the isotropic nominal value that would be expected in a purely ionic compound. All the deviations with respect to this reference *isotropic* nominal value are referred to as *anomalous*.

Focusing first on the deep Nb 4s and Li 1s levels, we do not identify any significant anomalous contribution, in agreement with the fact that these electrons do not participate to the bonding. To the contrary, the anomalous O 2p contribution is very large and mainly responsible for the total anomalous charge. This can be explained by dynamical changes of the Nb 4d orbital contribution to the O 2p bands producing a dynamical transfer of electrons from O to Nb when the Nb–O distance shortens. We note finally small and compensating anomalous contributions at the level of the Nb 4p and O 2s bands : they reveal the existence of hybridizations between these levels.

If we now compare the result in the paraelectric and in the ferroelectric phases in Table 1.6, we observe a global decrease of the charges in the ferroelectric state, specially along the ferroelectric direction. This is similar to what has been reported for the perovskite compounds. If we look at Table 1.8, we see that for Z^*_{Nb} this reduction originates in a modification of the O 2p contribution only. It confirms the strong influence of the phase

Bands	Nominal	paraelectric phase			ferroelectric phase		
Z_{core}	13.00	13.00	0	0	13.00	0	0
		0	13.00	0	0	13.00	0
		0	0	13.00	0	0	13.00
Nb 4s	-2.00	-2.04	0.03	0.00	-2.06	0.02	0.00
		-0.03	-2.04	0.00	-0.02	-2.06	0.00
		0.00	0.00	-2.02	0.00	0.00	-2.04
Li 1s	0.00	0.01	-0.01	0.00	0.01	-0.00	0.00
		0.01	0.01	0.00	0.00	0.01	0.00
		0.00	0.00	0.00	0.00	0.00	0.00
Nb 4p	-6.00	-6.42	-0.06	0.00	-6.49	-0.05	0.00
		0.06	-6.42	0.00	0.05	-6.49	0.00
		0.00	0.00	-6.37	0.00	0.00	-6.35
O 2s	0.00	0.57	0.09	0.00	0.60	0.10	0.00
		-0.09	0.57	0.00	-0.10	0.60	0.00
		0.00	0.00	0.58	0.00	0.00	0.50
O 2p	0.00	3.14	1.89	0.00	2.25	1.45	0.00
		-1.89	3.14	0.00	-1.45	2.25	0.00
		0.00	0.00	3.89	0.00	0.00	1.71
Total	5.00	8.26	2.07	0.00	7.30	1.62	0.00
		-2.07	8.26	0.00	-1.62	7.30	0.00
		0.00	0.00	9.08	0.00	0.00	6.83

Table 1.8: Band by band decomposition of the Born effective charge of the niobium atom (LDA calculation).

transition on the O 2p – Nb 4d hybridizations as discussed in Section 1.3.2. All the other contributions remain unaffected confirming that only the O 2p bands are affected by the phase transition.

In section 1.3.3, we had computed the spontaneous polarization of lithium niobate by using the Berry phase formulation proposed by King-Smith and Vanderbilt. From the tensors reported in Table 1.6, one can also access to a rough estimate of the spontaneous polarization by using the following formula :

$$P_{s,\alpha} = \frac{1}{\Omega_0} \sum_{\kappa,\beta} Z^*_{\kappa,\alpha\beta} \delta\tau_{\kappa,\beta} \tag{1.4}$$

where $\delta\tau_{\kappa,\beta}$ represents the displacement of atom κ during the phase transition. The calculation can be performed using the atomic positions reported in section 1.3.1 and keeping the lattice constants of the paraelectric phase. We obtain a value of 0.83 C/m^2 and 0.67 C/m^2 by using respectively the effective charges of the paraelectric and of the ferroelectric phase. At first, this illustrate that the reduction of Z^* has a strong effect on the magnitude of P_s. Moreover, comparing these values to the ones reported in Table 1.4, we see that the spontaneous polarization is not the mean of the two values estimated from the effective charges : this points out that the evolution of the charges along the ferroelectric path of atomic displacement is highly *non-linear*. A similar behaviour was observed for barium titanate [58].

1.5 Phonons

1.5.1 Paraelectric phase

The paraelectric phase belongs to the space group R$\overline{3}$c. At the Γ-point, the optical phonon modes can be classified according to its irreductible representations into:

$$\mathrm{A}_{1g} \oplus 2\mathrm{A}_{1u} \oplus 3\mathrm{A}_{2g} \oplus 3\mathrm{A}_{2u} \oplus 4\mathrm{E}_g \oplus 5\mathrm{E}_u.$$

The A_{2u} and E_u modes are infrared active. At the Γ point, they are split into transverse and longitudinal components A^T_{2u} (resp. E^T_u) and A^L_{2u} (resp. E^L_u). This splitting can be calculated from the Born effective charges and the optical dielectric tensor (see section 1.4.1) as it is described in Ref. [31].

The frequencies of the transverse and longitudinal modes are listed in Table 1.9. As no experimental data are available, we only compare our results to the frequencies calculated by Parlinski *et al.* [26]. Both calculations identify unstable A_{2u} and A_{2g} modes. Our calculated frequencies are usually in reasonnable agreement with those of Parlinsky *et al.* but there are exceptions, as for the E_g mode at 501 cm^{-1}. That could eventually be explained by strong anharmonicities of the potential energy to which our method is less sensitive. Another major difference is that the lowest E_u mode is unstable in our calculation whereas Parlinski *et al.* identify it as stable. The frequency of this mode is low, so that it is probably very sensitive to numerical errors. Anticipating what is

discussed at the end of this Section, we note that the instability of this mode is related to its giant effective charge and is therefore plausible.

Silent modes			Infrared active modes				
	Present	Ref. [26]		Present	Ref. [26]		Present
A_{1g}	403	415	A_{2u}^T	201i	227i	A_{2u}^L	90i
A_{1u}	279	294		94	116		346
	435	481		478	520		838
A_{2g}	115i	151i					
	405	393	E_u^T	53i	77	E_u^L	174
	889	912		177	152		274
E_g	175	162		393	411		419
	425	433		460	539		508
	501	617		532	614		844
	589	644					

Table 1.9: Phonon frequencies (in cm^{-1}) of the transverse and longitudinal modes in the paraelectric phase of lithium niobate.

At first, we note that it is the most unstable A_{2u} mode which drives the paraelectric to ferroelectric phase transition. The dynamical matrix eigenvector associated to this mode is

Li_1	(	0,	0,	0.466)
Nb_1	(	0,	0,	0.216)
O_1	(	0,	-0.050,	-0.276)
O_2	(	0.043,	0.025,	-0.276)
O_3	(	-0.043,	0.025,	-0.276).

It is worth noticing that it has an overlap of 0.99 with the vector representing the atomic displacements during the phase transition (for which we have chosen the same normalization as for the phonon eigenvectors).

On Figure 1.4 we have shown part of the phonon band structure in the paraelectric phase of $LiNbO_3$. We can identify three soft modes. The A_{2u} and A_{2g} modes are unstable in the whole Brillouin zone while the E_u mode gets stable away from the Γ-point.

To have a better insight on the microscopic origin of the different instabilities, we can use a model already applied by Ghosez *et al.* [56] to explain the phonon instability in barium titanate and which is based on a seminal idea of Cochran [60]. The interatomic forces in a crystal can be decomposed into short-range forces and a long-range Coulomb (dipole-dipole) interaction. A structural instability can appear from the cancellation of both contributions.

By following the notations of Ref. [56], we can write the full dynamical matrix A as the sum of a contribution due to the short-range forces (A_{SR}) and a contribution

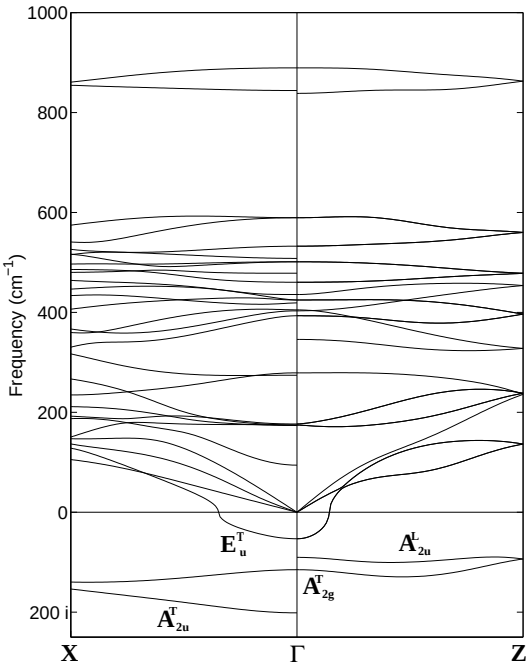

Figure 1.4: Phonon band structure in the paraelectric phase of $LiNbO_3$.

due to the dipole-dipole interactions (A_{DD}). The latter one can be evaluated by using Ewald summation techniques, as it is described in Ref. [61] whereas A_{SR} is obtained by subtracting A_{DD} from the full dynamical matrix A. Using this approach, we can decompose ω^2, as the sum of two contributions ω_{DD}^2 and ω_{SR}^2:

$$\underbrace{\langle\eta|A|\eta\rangle}_{\omega^2} = \underbrace{\langle\eta|A_{SR}|\eta\rangle}_{\omega_{SR}^2} + \underbrace{\langle\eta|A_{DD}|\eta\rangle}_{\omega_{DD}^2} \tag{1.5}$$

where η is an eigenvector of the full dynamical matrix. Table 1.10 gives the results of this decomposition for the three unstable modes of the paraelectric phase.

The A_{2u} mode that drives the phase transition is strongly destabilized by the dipole-dipole interactions that are not fully compensated by the short-range forces which tend to stabilize the paraelectric structure. The large amplitude of the dipolar interaction must be related to the high mode effective charge equal to 6.71 [1]. Similarly, the E_u mode at 53i cm^{-1} is strongly destabilized by the dipole-dipole interactions as we could expect from its even larger mode effective charge equal to 9.78. It is interesting to note that the square of

[1]For the mode effective charge Z_m^*, we use the same conventions as the authors of Ref. [31]:

$$Z_{m,\beta}^* = \left(\sum_{\kappa,\alpha} Z_{\kappa,\alpha\beta}^* \eta_{\mathbf{q}=0}^{(m)}(\kappa,\alpha)\right) / \left(\sqrt{\sum_{\kappa,\alpha}[\eta_{\mathbf{q}=0}^{(m)}(\kappa,\alpha)]^2}\right).$$

its frequency is the sum of two very large terms that do nearly cancel so that the resultant frequency is quite small.

	A_{2u} (201i)	A_{2g} (115i)	E_u (53i)
ω^2_{DD}	-88803	109023	-298387
ω^2_{SR}	48260	-122248	295571
ω^2	-40543	-13225	-2816

Table 1.10: DD and SR contributions to the TO mode frequency squared (cm^{-2}) for the soft modes in the paraelectric phase.

1.5.2 Ferroelectric phase

At the Γ-point, the optical phonons can be classified according to the irreductible representations of the space group R3c into :

$$4A_1 \oplus 5A_2 \oplus 9E.$$

The A_1 and E modes are Raman and infrared active so that they are split into transverse and longitudinal components.

A-modes

Tables 1.11 and 1.12 summarize the frequencies of the transverse and longitudinal A_1 modes that we have computed. Our results are compared to the frequencies calculated by Parlinski *et al.* [26] and Caciuc *et al.* [25] and to the experimental frequencies obtained by Raman and infrared spectroscopy. We note that the longitudinal frequencies reported by Parlinski *et al.* were obtained using an empirical guess of the Born effective charges and the optical dielectric tensor. The longitudinal modes have their wavevector along the z axis while the wavevectors of the transverse modes are perpendicular to it.

calc. frequencies			exp. frequencies		
present	Ref. [25]	Ref. [26]	Ref. [62]	Ref. [64]	Ref. [65]
243	208	239	252	251	252
288	279	320	275	273	276
355	344	381	332	331	333
617	583	607	632	631	634

Table 1.11: Phonon frequencies (in cm^{-1}) of the four transverse A_1 modes in the ferroelectric phase.

calc. frequencies		exp. frequencies		
present	Ref. [26]	Ref. [65]	Ref. [69]	Ref. [70]
287	309	273	275	273
348	381	306	333	332
413	548	423	436	436
855	831	869	876	873

Table 1.12: Phonon frequencies (in cm^{-1}) of the four longitudinal A_1 modes in the ferroelectric phase.

calc. frequencies			exp. frequency
present	Ref. [25]	Ref. [26]	Ref. [66]
218	153	220	224
297	287	321	314
412	417	432	
454	439	462	455
892	883	893	

Table 1.13: Phonon frequencies (in cm^{-1}) of the A_2 modes in the ferroelectric phase.

The calculated and measured frequencies of the A_2 modes are summarized in Table 1.13. Experimental data comes from inelastic neutron scattering [66]. Our results are quite close to the experimental data. They present in general a similar error as those obtained in previous calculations.

The A_1 mode at 234 cm^{-1} has the strongest overlap (0.82) with the A_{2u} mode that drives the phase transition in the paraelectric phase. By analysing the interatomic forces for this mode, we found $\omega^2_{DD} = -67649\ cm^{-2}$ and $\omega^2_{SR} = 126618\ cm^{-2}$ respectively. This helps us to clarify the stabilization of the soft mode after the phase transition. Although the Born effective charges decrease at the transition, the dipole-dipole interactions remain quite strong in the ferroelectric phase (strong enough to destabilize the mode in the paraelectric phase) and it is the increase of the short-range forces that stabilizes this mode. This behaviour contrasts with what was observed in barium titanate [56] where it is a decrease of the dipole-dipole interactions that stabilizes the ferroelectric mode in the rhombohedral phase.

E-modes

The analysis of the 9 E modes is more difficult. In the litterature, many different frequencies have been reported which where differently assigned. This comes from the fact that the properties of lithium niobate crystals strongly depend on the internal and external defects [21]. In particular, Raman spectroscopy is very sensitive to small modifications in

the structure and to the stoechiometry of the samples [63, 67].

For the transverse optic phonons, most authors seem to agree on seven modes around 152, 237, 265, 322, 368, 431 and 580 cm^{-1}. For the two missing modes, Ridah *et al.* [63] and Repelin *et al.* [67], suggest frequencies at 180 and 610 cm^{-1}, Kaminow *et al.* [68] report modes at 92 and 630 cm^{-1} and Claus *et al.* [69] mention phonons at 668 and 743 cm^{-1}. Barker *et al.* [65] are tempted to identify the modes at 180 and 610 cm^{-1} to mixed phonons that have their wavevector at 45^0 from the z axis and the mode at 670 cm^{-1} to a combination band. Yang *et al.* [70] report modes at 152 and 530 cm^{-1} and suggest that the frequencies at 741 and 667 cm^{-1} are due to combination bands.

For the transverse E modes, all the experimental values mentioned above as well as the theoretical results of Caciuc *et al.* [25] and Parlinski *et al.* [26] are summarized in Table 1.14 while the frequencies of the longitudinal E modes are given in Table 1.15.

Calc. frequencies			Exp. frequencies						
Present	Ref. [25]	Ref. [26]	Ref. [63]	Ref. [67]	Ref. [68]	Ref. [69]	Ref. [65]		Ref. [70]
					92				
155	151	157	153	155	152	155	152	152	152
	167		177	180					
218	236	214	238	238	238	238	236	238	236
264		269	264	265	262	265	265	264	263
330	307	349	322	325	322	325	322	321	322
	334								
372	352	419	369		368		363	367	
384		423		371		371			370
428	432	446	432	431	436	431	431	434	431
									530
585	526	605	580	582	582	582	586	579	578
	617		610	610					
					630				
677		690				668	670		
						743			

Table 1.14: Phonon frequencies (in cm^{-1}) of transverse E modes in the ferroelectric phase.

One can see that there are some discrepancies between the frequencies reported by the various authors. Even the previous first-principles calculations do not clarify all ambiguities. Parlinski *et al.*, whose results are relatively similar to ours, assign the seven modes reported by most authors as well as phonons at 423 and 690 cm^{-1}, while Caciuc *et al.* suggest the existence of phonons at 167 and 617 cm^{-1} as it was proposed by Ridah *et al.* and Repelin *et al.*. In order to clarify the identification of the E modes, we will analyze two quantities related to the phonon modes that have been measured experimentally in the past: the directional dispersion branches of the extraordinary phonons (Figure 1.5) and the mode oscillator strengths (Table 1.16).

Figure 1.5 shows the dependence of the phonon frequencies on the angle θ between the c axis and the phonon wavevector $\mathbf{q}$ in the limit of long wavelengths ($\mathbf{q} \rightarrow 0$). This

calc. frequencies		exp. frequencies			
présent	Ref. [26]	Ref. [65]	Ref. [69]	Ref. [70]	Ref. [63]
				152	186
197	204	198	198	194	195
224	216	238	243	240	240
298	316	296	295	295	299
349	372	342			345
384	422		371	370	
423	445	418	428	425	424
452	570	450	454	460	456
				530	
					625
675	677	660	668		
			739		
863	856	878	880	878	878

Table 1.15: Phonon frequencies (in cm^{-1}) of longitudinal E modes in the ferroelectric phase.

calculated directional dispersion relation agrees with the experimental measurements of Ref. [69, 70] for the branches (1)-(5) and (8)-(13). One main difference is the absence of branch (7) for both autors and the fact that they report a different behaviour for branch (6): according to their results, the A_{1L} mode transforms into an A_{1T} mode and not into an E_L mode as we have observed. Further differences concern branches at 743 [69] cm^{-1} and 152, 530 [70] cm^{-1} that are not reproduced by our calculation and that have not been found in the other experimental studies. We can thus assume that they are not related to first-order phonons.

On the basis of Figure 1.5 we will now discuss the assignation of selected phonon modes in Tables 1.14 and 1.15. Ridah *et al.* and Repelin *et al.* report an E_T mode at 180 cm^{-1} that has also been found by Caciuc *et al.* but not by Parlinski *et al.* neither in our study. As mentioned before, Barker *et al.* associate this frequency to a mixed phonon with the wavevector at 45^0 of the z axis. By looking at the spectra reported in the papers of Ridah *et al.* and Repelin *et al.* (Figure 3 of Ref. [63] and Figure 2 (b) of Ref. [67]), we see that this mode has indeed his wavevector in this direction (Ridah *et al.*, for example, measure it only in an X(ZY)Z orientation that allows them to detect transverse E modes whose wavevector form an angle of 45^0 with the z-axis). One can see from Figure 1.5 that the E_T mode at 155 cm^{-1} (branch (1)) transforms smoothly into the E_L mode at 197 cm^{-1} when θ varies from 0 to 90 degrees. At 45^0, the frequency of this mode is 174 cm^{-1} and it has a strong transverse component ($\mathbf{q}$ is along the direction (0,1,1)) as one can see it from its mode effective charge

$$\begin{pmatrix} 0 & -2.92 & 2.35 \end{pmatrix}.$$

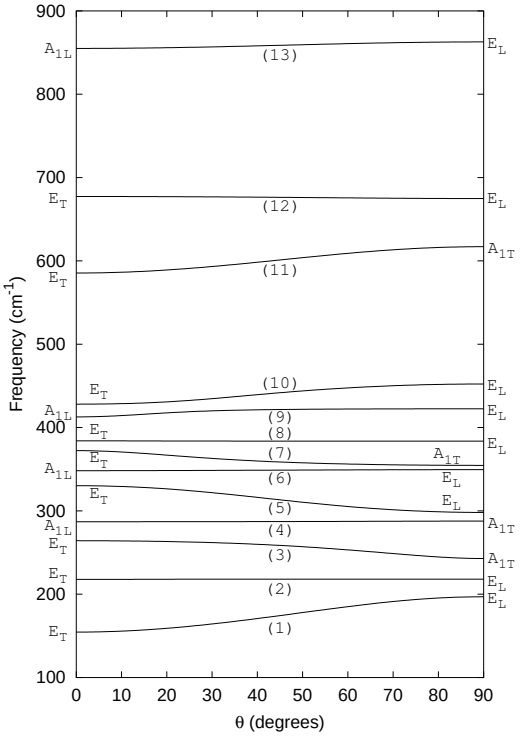

Figure 1.5: Directional dispersion branches of extraordinary phonons in the ferroelectric phase of $LiNbO_3$. θ is the angle between the c axis and the phonon wavevector $\mathbf{q}$.

Therefore, we believe that Ridah *et al.* and Repelin *et al.* have measured this particular mode and we propose that the second pure transverse E mode has in fact a frequency of 234 cm^{-1}, in agreement with the results of Parlinski *et al.*. We should note, that we observe a similar behaviour for branch (11): the E_T mode at 585 cm^{-1} gives rise to a mode of 601 cm^{-1} for $\theta = 45^0$. As Barker *et al.*, we are therefore tempted to assign the reported frequencies around 610 cm^{-1} to such a kind of mixed phonon and not to a pure transverse mode. [2]

One can see also from Table 1.14 that Caciuc *et al.* do not associate the measured mode at 264 cm^{-1} to any of their calculated phonons in spite of the fact that it has been observed in all the experiments cited above. They suppose that the measured line is due to a braking of the Raman selection rules caused by anharmonic effects and that it corresponds to the lowest A_{1T} mode. Their main argument is that Claus *et al.* have observed that this E_T mode transforms into the mentioned A_{1T} mode as θ varies from 0^0 to 90^0. But as can be seen from Figure 1.5, branch (3) reproduces this behaviour. As Parlinski *et al.* also find an E_T mode whose frequency is close to the measured one at 264

[2]For the sake of completeness, we should mention that this mode has not only been observed in an X()Z configuration as it is the case for the mode at 180 cm^{-1}, but also in an X()Y configuration that allows to measure phonons whos wavevector is in the plane perpendicular to the c axis. This argument holds thus less than for the mode at 180 cm^{-1}.

cm^{-1}, we conclude that it corresponds to a real first-order E_T phonon.

The last point we would like to discuss related to Figure 1.5 concerns the E_T modes at 372 and 384 cm^{-1}. In Table 1.14, they were associated to measured frequencies at 369 and 371 cm^{-1} that we believe to be related to two different phonons in spite of the fact that all other authors associate them to the same. The E_T and E_L modes at 384 cm^{-1} in Tables 1.14 and 1.15 correspond to branch (8) in Figure 1.5. This branch has been measured by Claus *et al.* and Yang *et al.* while line (7) is absent for both authors. Now, it is interesting to note that Ridah *et al.* and Barker *et al.* report a couple of E_T-E_L modes at 369 and 342 cm^{-1} that has not been reported by the two other autors but that can be found on Figure 1.5. Because of this fact, we suppose that the measured frequencies of 369 and 371 cm^{-1} correspond to two different first-order E_T modes that cannot been distinguished on the spectra due to the small difference in their frequencies.

A further certification of our assignement can be obtained from the inspection of Table 1.16 where we compare the mode oscillator strengths to the experimental values measured by Barker *et al.*. The mode oscillator strength $S_{m,\alpha\beta}$ for mode m was calculated from the

A_1 modes			E modes		
freq	S_m,calc	S_m,exp [65]	freq	S_m, calc	S_m,exp [65]
243	13.29	11.66	155	5.89	6.02
288	0.20	0.89	218	0.55	0.53
355	0.45	0.18	264	4.38	4.58
617	14.57	11.92	330	2.71	2.70
			372	3.59	3.59
			384	0.15	
			428	0.31	0.40
			585	14.33	13.43
			677	0.37	1.06

Table 1.16: Mode-oscillator strengths (in 10^{-4} atomic units) of the active modes in the ferroelectric phase of lithium niobate. For each mode, we also recall the calculated frequency.

Born effective charges and the phonon eigenvectors according to the relation:

$$S_{m,\alpha\beta} = \left(\sum_{\kappa,\gamma} Z^*_{\kappa,\gamma\alpha}\eta^{(m)}(\kappa,\gamma)\right)\left(\sum_{\kappa,\gamma} Z^*_{\kappa,\gamma\beta}\eta^{(m)}(\kappa,\gamma)\right). \tag{1.6}$$

For the A_1 modes, the agreement is reasonable. For most E modes, the agreement with experiment is much better except for the last mode. The Table shows in particular that the assumption concerning the E modes at 369 (372) and 371 (384) cm^{-1} is reasonable: Barker *et al.* report a mode oscillator strength of 3.59 for the mode at 369 cm^{-1}, in agreement with what we found for the mode at 372 cm^{-1}. The fact that they did not observe the mode at 371 cm^{-1} in their infrared measurements can also easily be understood because of its small mode oscillator strength.

On the contrary, Yang *et al.* as well as Claus *et al.* measured the mode at 371 cm^{-1} and they report that its frequency does not vary with θ. But if the frequencies of 369 and 371 cm^{-1} were related to the same phonon, the mode oscillator strength of 3.59 would give rise to a measurable angular dependence. This is another indication that the two frequencies measured on one side by Barker *et al.* and on the other side by Yang *et al.* cannot correspond to the same phonon.

Static dielectric tensor

In section 1.4.1, we have reported the optical dielectric tensor $\varepsilon^{\infty}_{\alpha\beta}$. This quantity describes the response of the electron gas to a homogenous electric field if the ions are taken as fixed at their equilibrum positions. To include the response of the cristal lattice to the electric field, one can use a model that assimilates the solid to a system of undamped harmonic oscillators [31]

$$\varepsilon^{0}_{\alpha\beta} = \varepsilon_{\alpha\beta}(\infty) + \frac{4\pi}{\Omega_0} \sum_m \frac{S_{m,\alpha\beta}}{\omega^2_m}. \tag{1.7}$$

The calculated and measured elements of $\varepsilon^{0}_{\alpha\beta}$ are summarized in Table 1.17. The agreement is very good for the elements ε^{0}_{xx} and ε^{0}_{yy} while ε^{0}_{zz} overestimates the experimental value. This result was predictable because we saw in the preceding section that

	reference	ε^0_{xx}	ε^0_{yy}	ε^0_{zz}
calc.	present	42.4	42.4	29.3
exp.	[65]	41.5	41.5	26.0
exp.	[70]	43.6	43.6	24.3

Table 1.17: Static dielectric tensor in the ferroelectric phase of lithium niobate.

the calculated mode oscillator strenghts agree better for the E modes than for the A_1 modes.

Looking back at Table 1.16, we observe that the two A_1 modes at 243 and 617 cm^{-1} have a large oscillator strength. However, due to their different frequency they do not contribute equally to ε^{0}_{zz}: the main contribution (84 %) comes from the A_1 mode at 243 cm^{-1} while only 14 % are originating in the mode at 617 cm^{-1}. For ε^{0}_{xx} and ε^{0}_{yy} we do not observe such a clear domination of one mode. The most important contributions come from the modes at 155 cm^{-1} (59 %), 264 cm^{-1} (15 %) and 585 cm^{-1} (10 %).

1.6 Conclusions

Using a plane wave pseudopotential approach to density functional theory, we studied structural, electronic, dielectric and dynamical properties of the two phases of lithium niobate. In particular, the amplitude of the optical dielectric tensor and of the Born effective charges have been obtained.

Some of our results were computed within a LDA and a GGA for the exchange-correlation energy. We found that the use of a GGA has only a small influence on quantities like the Born effective charges or the spontaneous polarization while it has a stronger impact on the optimized lattice parameters and atomic positions.

The analysis of the Born effective charges revealed several features that have already been observed in similar studies performed on perovskite oxydes: Z^*_{Nb} as well as Z^*_O are larger than their nominal ionic charge while Z^*_{Li} is rather close to it. The first two tensors decrease during the transition from the paraelectric to the ferroelectric phase while the latter one remains quite constant. All these results could be explained from the mixed ionic/covalent character of the chemical bonds in lithium niobate, especially from the partial hybridization between Nb 4d and O 2p states.

By examining the zone center phonons in the paraelectric phase, we have shown that a soft A_{2u} mode is responsible for the ferroelectric transition and from a model calculation we identified the destabilizing long-range dipolar forces to be at the origin of this phonon instability. During the discussion of the phonons in the ferroelectric phase, we paid much attention to the identification of the E modes. We tried to clarify the remaining ambiguities and we proposed a new assignation justified by the analysis of the mode oscillator strengths and of the angular dispersion relation of the extraordinary phonons.

Chapter 2

Electron localization: Band-by-band decomposition and application to oxides

Using a plane wave pseudopotential approach to density functional theory we investigate the electron localization length in various oxides. For this purpose, we first set up a theory of the band-by-band decomposition of this quantity, more complex than the decomposition of the spontaneous polarization (a related concept), because of the interband coupling. We show its interpretation in terms of Wannier functions and clarify the effect of the pseudopotential approximation. We treat the case of different oxides: BaO, α-PbO, $BaTiO_3$ and $PbTiO_3$. We also investigate the variation of the localization tensor during the ferroelectric phase transitions of $BaTiO_3$ as well as its relationship with the Born effective charges.

2.1 Introduction

In the study of periodic crystalline solids, the electronic ground-state wave function is usually described in terms of Bloch functions, delocalized on the whole system. As a consequence, for a long time, the understanding of electron localization in crystalline solids was mainly based on approximate pictures. Nevertheless, the basics of a quantitative characterization of electron localization had already been formulated by W. Kohn [71] in 1964. Recently this problematic was renewed, thanks to the development of the theory of polarization based on Berry phases [14, 15, 13, 72], and the rigorous definition of the position operator in periodic systems [73, 74, 75, 76]. These ideas have been further developped using a cumulant generating function approach [77].

Following these advances, Sgiarovello and co-workers [16], have computed the localization lengths for different cubic semiconductors, in the framework of the Kohn-Sham density functional theory [10, 11] (DFT). They showed that the degree of electron localization is quite different for the various investigated materials. These results encourage to pursue the study to other insulating crystals.

The localization tensor $\langle r_\alpha r_\beta \rangle_c$, can be computed from the periodic part of the Bloch functions $u_{nk}(\mathbf{r})$ and their first derivatives with respect to their wavevector :

$$\begin{aligned} \langle r_\alpha r_\beta \rangle_c &= \frac{V_c}{N(2\pi)^3} \int_{BZ} d\mathbf{k} \sum_{n=1}^{N} \left\{ \left\langle \frac{\partial u_{n\mathbf{k}}}{\partial k_\alpha} \middle| \frac{\partial u_{n\mathbf{k}}}{\partial k_\beta} \right\rangle \right. \\ &\quad \left. - \sum_{n'=1}^{N} \left\langle \frac{\partial u_{n\mathbf{k}}}{\partial k_\alpha} \middle| u_{n'\mathbf{k}} \right\rangle \left\langle u_{n'\mathbf{k}} \middle| \frac{\partial u_{n\mathbf{k}}}{\partial k_\beta} \right\rangle \right\} \end{aligned} \tag{2.1}$$

where V_c is the volume of the primitive unit cell, N the number of doubly occupied bands and α, β are two cartesian directions. The localization tensor is a *global* quantity that characterizes the occupied Kohn-Sham manifold as a *whole* (all k-points and all bands). This statement calls for two comments. First, applications of DFT to solids often make use of the frozen-core and pseudopotential approximations, while Eq.(2.1) requires an all-electron calculation. Second, the behavior of core and valence electrons is treated globally while both kinds of electrons are expected to exhibit strongly different localization properties interesting to identify independently.

The localization tensor has been shown [16] to give a lower bound for the spread of maximally localized Wannier functions (WF) as defined by Marzari and Vanderbilt [78, 79] (hereafter cited as MV). In order to get some insight into the physics of the chemical bonds in molecules and solids, such WF are usually constructed considering only a restricted number of electronic bands close to the Fermi level. The spread of the resulting WF is strongly dependent of the electronic states included in the minimization process. In this context, it seems interesting to try to identify the intrinsic localization of the electrons in a specific set of bands and to understand how this quantity is affected when including other bands. This would allow to solve the problem associated to the use of pseudopotentials and to characterize separately the behavior of core and valence electrons.

This chapter is organized as follows. In Sec. 2.2, we propose a decomposition of the localization tensor into contributions originating from isolated sets of bands composing the

energy spectrum of a solid. Using a simple model, we then illustrate the role of the covalent interactions on the different terms of the decomposition. We also make a connection between the localization tensor and the Born effective charges and we discuss the relation between pseudopotential and all-electron calculations. In Sec. 2.3, we give the technical details underlying our first-principles calculations and we point out the differences between our method and that applied in Ref. [16]. In Sec. 2.4 and 2.5, we present the results obtained on two ferroelectric perovskites ($BaTiO_3$ and $PbTiO_3$) as well as on two binary oxides (BaO and α-PbO). We investigate the variation of electron localization during the phase transitions of $BaTiO_3$ and show that the evolution is compatible with the electronic structure of this compound.

2.2 Band by band decomposition of the localization tensor

2.2.1 Formalism

Contrary to the polarization and the Born effective charges, for which band-by-band decompositions have been previously reported [81, 80, 58, 82], the localization tensor (Eq. (2.1)) involves scalar products between Bloch functions of different bands, making the identification of the contribution of isolated sets of bands less straightforward. In order to explain this fact, we have to remember that the localization tensor is related to the second moment of WF while the Born effective charges and the spontaneous polarization are linked to their first moment. From standard statistics, it is well known that these two quantities do not add the same way : when considering two random variables x_1 and x_2, the mean value of the sum $x_1 + x_2$ is simply the sum of the mean values while the variance of the sum is the sum of the variances *plus* an additional term, the covariance.

These considerations can be transposed in the simple context of a confined model system made of two orthonormalized states $\psi_1(x)$ and $\psi_2(x)$. The total many-body wavefunction $\Psi(x_1, x_2)$ is a Slater determinant constructed on the one-particle orbitals. The center of mass is given by the expectation value of the position operator $\hat{X} = \sum_{i=1,2} \hat{x}_i$

$$\overline{X} = \langle \Psi | \hat{X} | \Psi \rangle = \sum_{i=1,2} \langle \psi_i | \hat{x} | \psi_i \rangle \tag{2.2}$$

while the total spread (two times the localization tensor) is related to $\hat{X}^2$,

$$\begin{aligned} \sigma^2 &= \langle \Psi | \hat{X}^2 | \Psi \rangle - \langle \Psi | \hat{X} | \Psi \rangle^2 \\ &= \sum_{i=1,2} [\langle \psi_i | \hat{x}^2 | \psi_i \rangle - \langle \psi_i | \hat{x} | \psi_i \rangle^2] - 2 \langle \psi_1 | \hat{x} | \psi_2 \rangle \langle \psi_2 | \hat{x} | \psi_1 \rangle. \end{aligned} \tag{2.3}$$

We see that the first moments of the one-particle orbitals add to form the total dipole of the many-body wavefunction. On the contrary, the total spread is not equal to the sum of the individual spreads of ψ_1 and ψ_2 but involves also matrix elements of the one-particle position operator $\hat{x}$ between ψ_1 and ψ_2. The additional term would be absent if

the many-body wavefunction was a simple product of the one-particle orbitals. It arises from the anti-symmetry requirement. In analogy with the language of statistics, we will name it the *covariance*.

Based on these arguments, we can now define a band-by-band decomposition of Eq. (2.1). Suppose that the band structure is formed of N_g groups labelled G_i, each of them composed of n_i bands ($i = 1, ..., N_g$). The variance of a particular group G_i is defined as

$$\begin{aligned}\langle r_\alpha r_\beta \rangle_c(G_i) &= \frac{V_c}{n_i (2\pi)^3} \int_{BZ} d\mathbf{k} \left\{ \sum_{n \in G_i} \left\langle \frac{\partial u_{n\mathbf{k}}}{\partial k_\alpha} \middle| \frac{\partial u_{n\mathbf{k}}}{\partial k_\beta} \right\rangle \right. \\ &\left. - \sum_{n,n' \in G_i} \left\langle \frac{\partial u_{n\mathbf{k}}}{\partial k_\alpha} \middle| u_{n'\mathbf{k}} \right\rangle \left\langle u_{n'\mathbf{k}} \middle| \frac{\partial u_{n\mathbf{k}}}{\partial k_\beta} \right\rangle \right\} \end{aligned} \tag{2.4}$$

where the sums have to be taken over the bands of group G_i. The covariance of two groups G_i and G_j ($i \neq j$) is given by the following relationship:

$$\langle r_\alpha r_\beta \rangle_c(G_i, G_j) = \frac{-V_c}{n_i n_j (2\pi)^3} \int_{BZ} d\mathbf{k} \sum_{n \in G_i} \sum_{n' \in G_j} \left\langle \frac{\partial u_{n\mathbf{k}}}{\partial k_\alpha} \middle| u_{n'\mathbf{k}} \right\rangle \left\langle u_{n'\mathbf{k}} \middle| \frac{\partial u_{n\mathbf{k}}}{\partial k_\beta} \right\rangle . \tag{2.5}$$

Using these definitions, the total tensor, associated to the whole set of occupied bands, can be written as

$$\langle r_\alpha r_\beta \rangle_c = \frac{1}{N} \sum_{i=1}^{N_g} n_i \left\{ \langle r_\alpha r_\beta \rangle_c(G_i) + \sum_{j \neq i}^{N_g} n_j \langle r_\alpha r_\beta \rangle_c(G_i, G_j) \right\} . \tag{2.6}$$

The variance $\langle r_\alpha r_\beta \rangle_c(G_i)$ is intrinsic to an isolated set of bands. It is related [77, 16] to the quantity Ω_I introduced by MV through the relation

$$\Omega_I = n_i \sum_{\alpha=1}^{3} \langle r_\alpha r_\alpha \rangle_c(G_i). \tag{2.7}$$

In a one-dimensional crystal, Ω_I is simply the lower bound of the total spread Ω of the WF [1],

$$\Omega = \sum_{n \in G_i} [\langle r^2 \rangle_n - \langle r \rangle_n^2], \tag{2.8}$$

that can be realized by choosing an adequate phase factor for the Bloch functions. In a three-dimensional crystal, it is no more possible to construct WF that are simultaneously maximally localized in all cartesian directions. It is only possible to minimize their spread in one given direction as realized for the so-called hermaphrodite orbitals introduced in Ref. [16] : these particular functions are localized (Wannier-like) in a given direction α and delocalized (Bloch-like) in the two others. The variance of a particular group of bands $\langle r_\alpha r_\alpha \rangle_c(G_i)$ is the lower bound of the *average* spread $\frac{1}{n_i} \sum_{n \in G_i} [\langle r_\alpha^2 \rangle_n - \langle r_\alpha \rangle_n^2]$ where the sum is taken over all Wannier-like functions in the unit cell belonging to group G_i. This

[1] $\langle ... \rangle_n$ represents the expectation value over the n^{th} occupied Wannier function in the unit cell

lower bound is reached for WF that are maximally localized in direction α. The variance therefore gives some insight on the localization of the electrons within a specific set of bands taken independently. This localization is affected by the hybridizations between atomic orbitals giving rise to the formation of the considered electronic bands within the solid so that the variance can act as a probe to characterize these hybridizations.

The covariance is no more related to an isolated set of bands. It teaches us how the construction of WF including other bands can improve the localization. As discussed by MV, the definition of groups of bands in a solid is not unique and sometimes there is a doubt about which bands have to be considered together. If we consider two sets of bands G_i and G_j as one single group, its total variance is the sum of the individual variances *and* covariances, that have to be rescaled by the number of bands in each group

$$\langle r_\alpha r_\beta \rangle_c = \frac{1}{n_i + n_j} \left\{ n_i \left[\langle r_\alpha r_\beta \rangle_c(G_i) + n_j \langle r_\alpha r_\beta \rangle_c(G_i, G_j) \right] + n_j \left[\langle r_\alpha r_\beta \rangle_c(G_j) + n_i \langle r_\alpha r_\beta \rangle_c(G_j, G_i) \right] \right\}. \tag{2.9}$$

Until now, we considered separately the two cartesian directions α and β. Stronger results can be obtained when diagonal elements of the localisation tensor are considered, or when this localication tensor is diagonalized, and the eigenvalues are considered. Different inequalities can be derived. In particular, from Eq. (2.5), it appears that the covariances for $\alpha = \beta$ are always *negative*. This means that the diagonal elements of the full tensor are always smaller than those obtained by the sum of the diagonal variances. In other words, it is always possible to obtain more strongly localized orbitals by constructing WF considering more than one group of bands. As a consequence the covariance appears as a tool to identify which bands have to be considered together in the construction of WF in order to improve their localization.

In appendix A we give an interpretation of the variance and covariance in terms of the optical conductivity. It illustrates from a different viewpoint the influence of the fermionic nature of the electrons on the localization tensor : the appearance of the covariance in Eq. (2.6) is a direct consequence of the Pauli principle.

2.2.2 Simple model

In this section we will investigate a one-dimensional model system. This will help us to understand the role of the covalent interactions on the electron localization length and related quantities like the Born effective charges. We will deal with a confined system for which the localization tensor can be computed from matrix elements of the position operator and its square as described in Ref. [16].

Let us consider a diatomic molecule XY. In order to describe the chemical bonds of this model system we adopt a tight-binding scheme [59] defined by the hopping integral t and the on-site terms Δ and $-\Delta$. We will call a the interatomic distance and ψ_X, ψ_Y the s-like atomic orbitals that are used as basis functions. The hamiltonian can be rescaled by Δ (A=t/Δ) in order to become a one parameter hamiltonian defined by

$$H = \begin{pmatrix} -1 & A \\ A & 1 \end{pmatrix}. \tag{2.10}$$

We further assume that ψ_X is centered at the origin, ψ_Y in a and that these two functions do not overlap at any x

$$\psi_X(x)\psi_Y(x-a) = 0. \tag{2.11}$$

The eigenfunctions of the hamiltonian correspond to

$$\phi_{1,2}(x) = u_{1,2}\psi_X(x) + v_{1,2}\psi_Y(x-a) \tag{2.12}$$

where the coefficients $u_{1,2}$ and $v_{1,2}$ can be expressed in terms of the bond polarity [59] α_p ($\alpha_p = \frac{1}{\sqrt{1+A^2}}$):

$$\begin{aligned} u_1 &= \sqrt{\tfrac{1+\alpha_p}{2}}, \quad v_1 = \sqrt{\tfrac{1-\alpha_p}{2}} \\ u_2 &= \sqrt{\tfrac{1-\alpha_p}{2}}, \quad v_2 = -\sqrt{\tfrac{1+\alpha_p}{2}}. \end{aligned} \tag{2.13}$$

In order to see the meaning of the different terms appearing in the band by band decomposition of the localization tensor and the Born effective charges let us first consider the molecular orbitals independently.

The variance of state ϕ_1 can be computed from the coefficients u_1 and v_1. It writes

$$\langle x^2 \rangle_c(1) = \sigma_X^2 \frac{1+\alpha_p}{2} + \sigma_Y^2 \frac{1-\alpha_p}{2} + \frac{a^2 A^2}{4(1+A^2)} \tag{2.14}$$

where σ_X^2 and σ_Y^2 are the second central moments of ψ_X and ψ_Y. The variance of ϕ_2 is given by a similar expression. This quantity is composed of three positive terms that summarize the mechanisms that are able to delocalize the electrons with respect to the atomic orbitals. On one hand, the electronic cloud on a particular atom is not a delta-Dirac function but presents a degree of delocalization related to σ_X^2 and σ_Y^2 (first and second term). When the state ϕ_1 is made entirely of ψ_X, that is, when α_p equals one, the localization length is correctly equal to σ_X^2 (first term). Incorporating more ψ_Y changes the localization length in proportion of α_p (the balance between first and second terms). On the other hand, the electrons can occupy two sites X and Y that are separated by a distance a (third term). This term scales as a^2. Even a small covalent interaction is thus able to induce an important delocalization if it acts on a sufficiently large distance.

The Born effective charge of atom X is defined as the derivative of the dipole moment p with respect to a. This dipole moment is the sum of the nuclear and static electronic charges multiplied by the interatomic distance. The contribution coming from the electrons occupying state ϕ_1 is equal to

$$p_1 = -2eu_1^2 a = -e(1+\alpha_p)a \tag{2.15}$$

where e is the module of the electronic charge. The derivative of Eq. (2.15) with respect to a gives the contribution of these electrons to the total effective charge

$$Z^*_{X,1} = \frac{\partial p_1}{\partial a} = -e(1+\alpha_p) + ea\frac{A}{(1+A^2)^{3/2}}\frac{\partial A}{\partial a}. \tag{2.16}$$

The first term is the (static) effective atomic charge [59] of atom X while the second term represents an additional dynamical contribution due to a transfer on electrons between X

and Y during a relative atomic displacement. The contribution of the electrons occupying state ϕ_2 is given by a similar expression

$$Z^*_{X,2} = \frac{\partial p_2}{\partial a} = -e(1-\alpha_p) - ea\frac{A}{(1+A^2)^{3/2}}\frac{\partial A}{\partial a}. \tag{2.17}$$

This simple model illustrates how both the variance of the localization tensor and the Born effective charges depend on the covalent interactions defined by the parameter A. The variance is a *static* quantity depending on the amplitude of the covalent interations only while the the Born effective charges are *dynamical* quantities that also depend on the variations of these interactions during a relative atomic displacement.

If we now consider the states ϕ_1 and ϕ_2 as a single group we have to add their variances and covariances to get the whole localization tensor. The covariance reduces to

$$\langle x^2\rangle_c(1,2) = \frac{-a^2A^2}{4(1+A^2)}. \tag{2.18}$$

By adding this covariance to the variance in Eq. (2.14), we remove in some sense the delocalization induced by the covalent interactions. The total localization tensor becomes independent of the hopping A and the interatomic distance a. It reduces to the mean spread of the atomic orbitals ψ_X and ψ_Y :

$$\langle x^2\rangle_c = \frac{\sigma^2_X + \sigma^2_Y}{2}. \tag{2.19}$$

Eq. (2.19) defines the mean spread of the WF constructed as linear combinations of ϕ_1 and ϕ_2 that minimize the spread functional Ω (see Eq. (2.8)). As shown by MV, these WF diagonalize the position operator $\hat{x}$ projected on the subspace of occupied states. They are thus equal to the atomic orbitals since the hypothesis of zero overlap (Eq. (2.11)) implies $\langle\psi_X|\hat{x}|\psi_Y\rangle = 0$.

The total Born effective charge of atom X can be obtained by adding the nuclear charge $Z^*_{core} = 2e$ to the terms (2.16) and (2.17). It is easy to check that for this model Z^*_X is equal to zero. This result can be interpreted in two ways. The point of view usually adopted is to say that the two molecular orbitals are of the opposite polarity so that the total dipole of the molecule vanishes. Based on the results of the preceeding paragraph, we can also affirm that each maximally localized WF is confined on a single atom so that no interatomic charge transfer can take place.

This result suggests that the variance gives more informations about the localization of electrons of particular chemical bonds than the total localization tensor. It also illustrates the observation of Ghosez *et al.* [58, 81] that anomalous effective charges mainly come from hybridizations between occupied and unoccupied states. In fact, the different chemical bonds generate opposite effects so that a net charge transfer is possible only if some of them are unoccupied.

In summary, we have illustrated the mechanisms that govern the variance of the localization tensor and the Born effective charges in the particular case of a one dimensional

model system. The observations made in this section give us an intuitive understanding of how delocalized electrons can generate *anomalous* effective charges. Hybridizations between occupied states generate opposite effects that tend to cancel out when they are summed. Because of the simplicity of the above adopted picture, we have however to be careful when we apply this model to real materials. First, we considered only hybridizations between two types of atomic orbitals, while the chemical bonds in real systems generally result from more complicated interactions. In particular, we neglected on-site hybridizations that are also able to generate *anomalous* effective charges but that induce a stronger localization on the electronic cloud. Second, the hypothesis of zero overlap (2.11) is not always fullfilled so that maximally localized WF constructed on the whole set of occupied states generally not reduce to the atomic orbitals. Nevertheless, this simple model will allow us to interpret some results in Sections 2.4 and 2.5.

2.2.3 Pseudopotentials

As mentioned in the introduction, there is a fundamental problem in the computation of the total localization tensor when pseudopotentials are used. This is due to the fact that the localization tensor is related to the bands of the system as a whole : first, there is no cancellation between the core electrons and the nuclear charge, as it is the case in the computation of the total polarization; second, the localization tensor is a kind of mean over all bands, that combines strongly localized (core) states, and weakly localized (valence) states. This is clearly seen in Eq.(2.1), where the number of bands explicitely appears both as the denominator of the prefactor and in the two summations. The band-by-band decomposition allows us to overcome this problem partly, by focusing only on the variances of isolated groups of bands. Thanks to Eq. (2.9) it is also possible to get some insight into the physics of the all-electron localization tensor when pseudopotentials are used. In this section, we focus on the diagonal elements of the electron localization tensor $\alpha = \beta$ (of course, any direction can be chosen as α).

In an all-electron calculation, let us consider separately two sets of bands: core bands (labelled as 'co'), and valence bands (labelled as 'va'). The total localization tensor can be obtained from the localization tensors of each group of bands, combined with the covariance between the two groups of bands:

$$\langle r_\alpha r_\alpha \rangle_c = \frac{1}{n_{co} + n_{va}} \left\{ n_{co} \langle r_\alpha r_\alpha \rangle_c(co) + n_{va} \langle r_\alpha r_\alpha \rangle_c(va) + 2 n_{co} n_{va} \langle r_\alpha r_\alpha \rangle_c(co, va) \right\}. \quad (2.20)$$

Both variances $\langle r_\alpha r_\alpha \rangle_c(co)$ and $\langle r_\alpha r_\alpha \rangle_c(va)$ are positive quantities. The covariance times the product of the number of bands $n_{co} n_{va} \langle r_\alpha r_\alpha \rangle_c(co, va)$, a negative quantity, must always be smaller in magnitude than each of the related variances multiplied by the corresponding number of bands. This translates to bounds on the diagonal elements of the total localization tensor :

$$\frac{|n_{va} \langle r_\alpha r_\alpha \rangle_c(va) - n_{co} \langle r_\alpha r_\alpha \rangle_c(co)|}{n_{co} + n_{va}} \leq \langle r_\alpha r_\alpha \rangle_c \leq \frac{n_{va} \langle r_\alpha r_\alpha \rangle_c(va) + n_{co} \langle r_\alpha r_\alpha \rangle_c(co)}{n_{co} + n_{va}}. \quad (2.21)$$

In the frozen-core approximation, $\langle r_\alpha r_\alpha \rangle_c(co)$ can be obtained from separate all-electron calculations for each atom of the system. The localization tensor of the valence bands is (likely) computed accurately in the pseudopotential approximation : the spread of the Wannier functions should be quite similar if estimated from all-electron valence wavefunctions or from pseudo-wavefunctions.

Thus, a *bound* on the diagonal elements of the localization tensor *can be computed* from the atomic wavefunctions of the core electrons and the pseudo-valence wavefunctions. In order to compute the covariance more accurately it is necessary to reconstruct the all-electron wavefunctions. This could be done following the ideas exposed in Ref. [88].

2.3 Method and implementation

In the remaining part of this paper, we apply the previous formalism to various oxides. The electronic wavefunctions are obtained within DFT [10, 11] and the local density approximation (LDA) thanks to the ABINIT [27] package. At variance with a previous work on semiconductors [16], the first derivatives of the wave functions with respect to their wavevector are not computed from finite differences but from a linear-response approach [32] within the parallel-transport gauge. The wave functions are further transformed to the diagonal gauge [82]. Both ground-state and first-order wavefunctions are expanded in plane waves up to a kinetic-energy cutoff of 45 Hartree. Integrations over the BZ are replaced by sums over a $8 \times 8 \times 8$ mesh of special k-points [37]. With these parameters, the convergence of the localization tensor for the investigated compounds is better than 10^{-3} Bohr^2. The ionic-core electron potentials of the Ba, Pb, Ti and O atoms are replaced by ab initio, separable, extended norm-conserving pseudopotentials, as proposed by M. Teter [84]. Ba 5s, 5p and 6s electrons, Pb 6s, 5d and 6p electrons, Ti 3s, 3p and 3d electrons, O 2s and 2p electrons are considered as valence states. Beside calculating the localization tensor on bulk-materials, we also computed it on the isolated atomic systems Ba^{2+}, Pb^{2+} and O by placing each atom at the origin of a periodic supercell of 20 Bohrs.

As shown by Sgiarovello *et al.* [16], the localization tensor and thus the variances and covariances, are real. Moreover, they are obviously symmetric in α and β. Consequently there exists a set of cartesian axes where they are diagonal and their eigenvalues are also real numbers. In the discussion of our results we will always work in this particular frame so that we do not need to consider the off-diagonal elements of the localization tensor.

2.4 Results

2.4.1 Structural and electronic properties

We will consider the two binary oxides BaO and α-PbO as well as the ferroelectric perovskites $BaTiO_3$ and $PbTiO_3$. BaO has a rocksalt structure while the tetragonal α phase of lead oxide is formed of parallel layers of Pb and O atoms. $BaTiO_3$ and $PbTiO_3$ have a

high-temperature cubic perovskite structure with five atoms per unit cell. As the temperature is lowered, the former compound undergoes a sequence of three ferroelectric phase transitions transforming to tetragonal, orthorhombic and rhombohedral structures while the latter compound only undergoes one single transition from the cubic to the tetragonal phase. We will consider explicitely the cubic, tetragonal and rhombohedral phases of $BaTiO_3$ as well as the cubic phase of $PbTiO_3$.

The electronic structures of these compounds have been previously studied [80, 85, 87, 43] and are illustrated in Fig. 2.1. They are formed of well separated groups of bands. Each of them has a marked dominant orbital character and can be labeled by the name of the atomic orbital that mainly composes the energy state in the solid. The bands at the Fermi level are mainly composed of O 2p states that show significant interactions with other atomic orbitals like the well known O 2p-Ti 3d hybridization in $BaTiO_3$ and $PbTiO_3$. The bandstructures in the ferroelectric phases of $BaTiO_3$ are similar to that of the cubic phase. The phase transitions principally affect the bandgap and the spread of the O 2p bands while the positions of the deeper lying bands remain quite constant. The main difference in the electronic structures of BaO and $BaTiO_3$ on one hand and PbO and $PbTiO_3$ on the other hand comes from the presence or absence of Pb 6s electrons (that form the so called lone-pair in PbO). These electrons show a strong hybridization with the O 2p states. As a consequence the O 2p and Pb 6s bands are degenerate at the R point in $PbTiO_3$ and around the Z point in PbO. Consequently, we have to consider them as one single group of bands in the decomposition of the localization tensor.

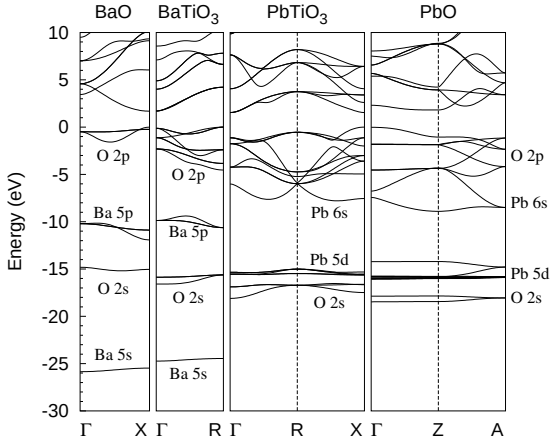

Figure 2.1: Band structures of BaO, cubic $BaTiO_3$, cubic $PbTiO_3$ and α-PbO.

2.4.2 Localization tensor and Born effective charges

As the total localization tensor is meaningless in pseudopotential calculations that do not include covariances with the core states, we focus on the variances of the different groups

of bands. The values can be found in the Tables 2.1 and 2.2 where they are compared to the variances of the dominant atomic orbitals. We do not report any values associated to the deepest lying Ti 3s and Ti 3p bands although they have been included in our pseudopotential calculation. Their variances are in fact close to the atomic ones and they do not show any sizeable covariance with other bands in both $BaTiO_3$ and $PbTiO_3$.

System	Str.	Element	Band			
			Ba 5s	O 2s	Ba 5p	O 2p
Atom	–	$\langle r^2 \rangle_c$	1.011	0.929	1.370	–
BaO	–	$\langle r^2 \rangle_c$	1.065	1.552	2.023	2.199
$BaTiO_3$	C	$\langle r^2 \rangle_c$	1.091	0.950	2.189	1.875
	T	$\langle r^2_\perp \rangle_c$	1.091	0.945	2.180	1.852
		$\langle r^2_\parallel \rangle_c$	1.088	0.965	2.175	1.842
	R	$\langle r^2_\perp \rangle_c$	1.092	0.963	2.196	1.862
		$\langle r^2_\parallel \rangle_c$	1.092	0.949	2.189	1.804

Table 2.1: Variances (Bohr^2) of the Ba 5s, O 2s, Ba 5p and O 2p bands for the isolated atomic systems Ba^{2+} and O, BaO and the cubic (C), tetragonal (T) and rhombohedral (R) phases of $BaTiO_3$.

System	Element	Band		
		O 2s	Pb 5d	Pb 6s + O 2p
Atom	$\langle r^2 \rangle_c$	0.929	0.657	–
$PbTiO_3$	$\langle r^2 \rangle_c$	1.874	1.490	1.749
PbO	$\langle r^2_\perp \rangle_c$	2.234	1.142	2.178
	$\langle r^2_\parallel \rangle_c$	1.724	0.990	1.968

Table 2.2: Variances (Bohr^2) of the O 2s, Pb 5d and Pb 6s +O 2p bands in $PbTiO_3$, α-PbO and for the isolated atomic systems Pb^{2+} and O.

In the cubic crystals BaO, $BaTiO_3$ and $PbTiO_3$ as well as in the atomic systems, the reported tensors are isotropic so that we only mention their principal values $\langle r^2 \rangle_c$. This is no more true in the ferroelectric phases of $BaTiO_3$ where a weak anisotropy can be observed. The tensors have an uniaxial character as the corresponding dielectric ones: they are diagonal when expressed in the principal axes and the elements $\langle r^2_\perp \rangle_c$ and $\langle r^2_\parallel \rangle_c$ refer to cartesian directions perpendicular and parallel to the optical axis (that has the direction of the spontaneous polarization). A much stronger anisotropy is observed in α-PbO where the localization tensor has the same symmetry as in the ferroelectric phases of $BaTiO_3$. Due to its particular structure formed of atomic Pb-O planes the electrons of each group of bands are more delocalized in a direction parallel ($\langle r^2_\perp \rangle_c$) to the atomic

planes[2] than perpendicular ($\langle r_{\parallel}^2 \rangle_c$) to them. This observation agrees with our intuitive picture that the covalent interactions between atoms inside a layer are stronger than between atoms of different layers.

Examining the variances of the different groups of bands we see that the Ba 5s electrons show a similar degree of localization both in BaO and $BaTiO_3$ also equivalent to that of the corresponding atomic orbital. On the contrary, the O 2s electrons behave differently in the materials under investigation: in $BaTiO_3$, their variance is close to the atomic one while they show a significant larger delocalization in the three other compounds. It is in fact surprising to see the degree of delocalization of the inner bands like the O 2s, Ba 5p or Pb 5d bands. In some cases like $BaTiO_3$, the electrons of these bands are even more strongly delocalized than those of the bands at the Fermi level. These results suggest that the corresponding atomic orbitals are chemically not inert but present non negligible covalent interactions. An interesting observation can be made for the O 2s and Pb 5d bands in $PbTiO_3$ and α-PbO. The delocalization induced by the covalent interactions that generate these bands tends to disappear when we consider them as one single group. In order to compute the variance of the whole O 2s and Pb 5d bands, we have to use Eq. (2.9). As an example let us consider $PbTiO_3$. The different elements can be summarized in a matrix where the diagonal elements are the variances (Bohr^2) and the off-diagonal elements the covariances (Bohr^2) of the individual groups

$$\begin{pmatrix} 1.874 & -0.240 \\ -0.240 & 1.490 \end{pmatrix}.$$

The total variance of the (O 2s + Pb 5d) group considered as a whole reduces to 0.734 Bohr^2. For α-PbO, we obtain similar values of 0.732 Bohr^2 for $\langle r_{\perp}^2 \rangle_c$ and 0.701 Bohr^2 for $\langle r_{\parallel}^2 \rangle_c$. These values can be compared to the mean spread of the atomic orbitals $\frac{1}{6}(0.929 + 5 \times 0.657) = 0.702$ Bohr^2.

The results presented above suggest that inner orbitals like O 2s, Ba 5p or Pb 5d are chemically not inert in the materials under investigation. This observation seems in contradiction with the conclusions drawn from partial density of states analysis [87] that these states are rather inert. Nevertheless the inspection of the Born effective charges in BaO or $BaTiO_3$ [80, 81] confirms our observations that will now be illustrated for α-PbO and $PbTiO_3$. This points out that the global shape of the bandstructure is less sensitive to the underlying covalent interactions than the variance of the localization tensor or the Born effective charges.

In order to investigate the connection between the localization tensor and the Born effective charges we report in Table 2.3 the band by band decomposition of Z_{Pb}^* in $PbTiO_3$ and α-PbO. In the perovskite, this tensor is isotropic while in α-PbO it has the same symmetry as the localization tensor. The contribution of each group of bands has been separated into a reference nominal value and an *anomalous* charge[3]. For α-PbO, we ob-

[2] In α-PbO, the optical axis is perpendicular to the atomic layers.

[3] The Born effective charges are in general compared to an isotropic nominal value that is the charge expected in a purely ionic compound. All deviations with respect to this reference nominal value are referred to as *anomalous*.

serve the same anisotropy as for the localization tensor: the covalent interactions inside an atomic layer ($Z^*_{Pb\perp}$) generate larger *anomalous* contributions than the interactions involving atoms of different layers ($Z^*_{Pb\parallel}$). By looking at the O 2s and Pb 5d bands we see that they generate important anomalous charges that confirm our observations concerning the variances of these bands. Interestingly, in both materials these contributions cancel out when they are summed. We observe thus the same tendencies for the Born effective charges and the localization tensor: the effects induced by the covalent interactions between inner orbitals tend to disappear when the resulting bands are considered together.

	$PbTiO_3$	α-PbO	
Band	Z^*_{Pb}	$Z^*_{Pb\perp}$	$Z^*_{Pb\parallel}$
Core	14.00	14.00	14.00
O 2s	0 + 3.47	0 + 1.89	0 + 0.26
Pb 5d	-10 - 3.36	-10 - 1.80	-10 - 0.40
Pb 6s + O 2p	-2 + 1.78	-2 + 1.06	-2 + 0.48
Tot.	2 + 1.89	2 + 1.15	2 + 0.34

Table 2.3: Band by band decomposition of the Born effective charges (a. u. of charge) in $PbTiO_3$ and α-PbO. The contributions have been separated into a reference nominal value and an *anomalous* charge.

2.5 Discussions

Based on the simple model exposed in Sec. 2.2.2 we can suggest the following mechanism to explain the results presented in the preceeding section. The atomic orbitals O 2s and Pb 5d (for which the hypothesis of zero overlap (2.11) is reasonable) present weak covalent interactions that generate the corresponding energy bands in $PbTiO_3$ and α-PbO. When we construct maximally localized WF for each individual group, the resulting orbitals are delocalized on Pb and O atoms so that during an atomic displacement an interatomic transfer of charges − generating *anomalous* Born effective charges − is possible. The fact that the variance of the global (O 2s + Pb 5d) group of bands is close to the mean spread of the atomic orbitals suggests that the maximally localized WF constructed on these bands are similar to the original atomic orbitals. In other words, they are confined on a single atom. This confinement also suppresses the interatomic charge transfer so that the anomalous charges disappear. We can make similar observations for the Ba 5p and O 2s bands in BaO and $BaTiO_3$, although, in the latter compound, the cancellation in the Born effective charges and the variance is not as complete as in the three remaining ones. This suggests that in the lead oxides as well as in BaO, the inner bands Pb 5d and O 2s (resp. Ba 5p and O 2s) mainly result from hybridizations between two types of atomic

orbitals. At the opposite, in $BaTiO_3$ the Ba 5p and O 2s bands are formed of more than two types of atomic orbitals.

Looking now at the bands at the Fermi level, we see that their variance is significantly larger in BaO and α-PbO than in the corresponding perovskites and that it remains nearly constant in the different phases of $BaTiO_3$. This latter observation seems surprising for two reasons. (i) The LDA bandgap presents drastic changes when passing from the cubic (1.72 eV) to the rhombohedral (2.29 eV) phase. This increase suggests a much stronger localization of the O 2p electrons in the ferroelectric phases. (ii) The giant Born effective charges observed in the paraelectric phase [58, 81] imply an important reorganization of the electronic cloud during an atomic displacement. It appears surprising that this reorganization has such small effects on the localization tensor. These small variations are not restricted to $BaTiO_3$ but similar observations have been made in other ferroelectric compounds like $LiNbO_3$ [89].

Considering point (i), we note that the correlation between the bandgap and the localization tensor is not as tight as one might think. The variance of the O 2p bands for instance is significantly larger in BaO than in $BaTiO_3$ in spite of the fact that its LDA bandgap (1.69 eV) is close to the gap in the cubic phase of $BaTiO_3$.

Considering point (ii), we note that it is possible to have an important reorganization of the electronic charge *without* affecting the localization tensor a lot. Following the ideas of the Harrison model [59], the giant effective charges in perovskite ferroelectrics result from dynamical orbital hybridizations changes generating interatomic transfers of charges. In Fig. 2.2 (a) we have drawn shematically an O centered WF in the cubic phase of $BaTiO_3$ along a Ti - O chain. Due to the O 2p - Ti 3d hybridization, this WF has a finite probability on the neighbouring Ti_1 and Ti_2 atoms. According to the Harrison

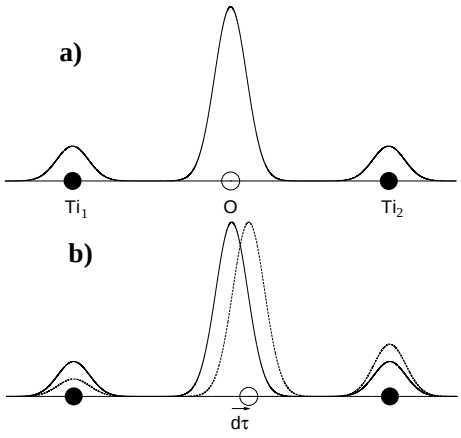

Figure 2.2: Oxygen centered WF in the cubic phase (solid line) of $BaTiO_3$ (a) and its variation during the transition to the tetragonal phase (dashed line) (b).

model, a fraction of electrons is transferred from Ti_1 to Ti_2 during a displacement $d\tau$ of the O atom (Fig. 2.2 (b)). Even if the quantity of charges involved in this process is small, the large scale on which this transfer takes place (of the order of the lattice parameter)

implies a shift of the WF center larger than the underlying atomic displacement and explains the *anomalous effective charges*. During the transition from the cubic to the tetragonal phase, the central O atom is displaced by few percents of the lattice constant a ($\frac{d\tau}{a} = 0.045$) with respect to Ti_1 and Ti_2. The resulting shift of the WF center generates the spontaneous polarization in the ferroelectric phase.

Based on this simple picture the origin of the small variations of the O 2p variance during the phase transitions becomes more obvious: When the electrons are transferred from Ti_1 to Ti_2 their distance to the initial WF center remains unaffected and their distance to the displaced WF center slightly decreases due to its shift towards Ti_2. Mathematically speaking, due to the fact that the variations do not depend on the direction of the atomic displacement, they are of the second order in $\frac{d\tau}{a}$.

In order to get a numerical estimate of the charges transferred during this process and its impact on the localization tensor we can consider a one dimensional model WF whose square is the sum of three delta-Dirac functions

$$|W_n(x)|^2 = \frac{1}{2}\left\{\frac{2 - Z'_O}{2}\left[\delta(x-a) + \delta(x+a)\right] + Z'_O\delta(x)\right\}. \tag{2.22}$$

This model only takes into account the delocalization of the electrons on different atoms (third term of Eq. (2.14)) while it completely neglects the delocalization of the electronic cloud on the individual atoms (first and second term of Eq. (2.14)). In this particular case we can identify the localization tensor to the second moment of the WF. This is no more true in a real, three dimensional crystal. In $BaTiO_3$ for instance, the O 2p group contains 9 different WF per unit cell located on three different O atoms. These WF extend in different spatial directions so that their *average* spread in the x-direction is lower than the spread of one single WF as the one shown in Fig. 2.2.

In Eq. (2.22), Z'_O represents the probability of the electrons to be found on the O atom. It can be computed from the value of the O 2p variance in the paraelectric phase of $BaTiO_3$ and the lattice constant a using the relation $\int x^2|W_n(x)|^2dx = \langle r^2\rangle_{c,O2p}$. This yields $Z'_O = 1.73$. This quantity allows an estimate of the static charge of the O atom in $BaTiO_3$ by substracting three times Z'_O from the charge due to the nucleus and the core electrons O 1s and O 2s. This yields $Z_{O,st} = 4 - 3 \cdot 1.73 = -1.19\ e$.

When the O atom is displaced, the shift of the WF center is directly related to the quantity of charges ε transferred from Ti_1 to Ti_2. The value of ε can be computed from the value of the effective charge generated by the O 2p electrons ($Z^*_{O2p} = -9.31$) in the cubic phase [58] by taking into account that the *anomalous* charges are generated by three WF located on the same O atom [79]. To get the polarization due to one single WF, we have to divide this quantity by 3 since each of them brings a similar contribution to Z^*_{O2p}. In the tetragonal phase, the model WF writes

$$|W_n(x)|^2 = \frac{1}{2}\left\{\frac{2 - Z'_O - \varepsilon}{2}\delta(x+a) + Z'_O\delta(x - d\tau) + \frac{2 - Z'_O + \varepsilon}{2}\delta(x-a)\right\}. \tag{2.23}$$

By identifying twice its first moment to $Z^*_{O2p}d\tau/3$ one gets $\varepsilon = 0.0614$ at the transition from the cubic to the tetragonal state. It implies a decrease in the spread of the model WF of 0.18 $Bohr^2$.

This variation is larger than the observed one (0.023 Bohr^2). Part of the discrepancy is probably due to the fact that we considered Z^*_{O2p} to be constant along the path of atomic displacement from the paraelectric to the ferroelectric phase. Using the value of Z^*_{O2p} in the tetragonal phase we obtain a value of 0.0467 for ε while the variance decreases of 0.12 Bohr^2. Moreover, one has to bear in mind that the localization tensor in $BaTiO_3$ is an average value that has to be taken over 9 WF. Six of them are centered on O atoms that ly in a plane perpendicular to the direction of the spontaneous polarization. They are probably less affected by the phase transition. As a consequence, the variation of the WF located on the remaining O atom (the one represented on Fig. 2.2) is expected to be larger than the variation of the localization tensor.

In summary, even if there is no formal connection between the real WF in $BaTiO_3$ and Eq. (2.22), this simple model shows that small variations of the localization tensor are compatible with giant effective charges and their interpretation in terms of the Harrison model. As illustrated with the model WF, the transfer of charges along the Ti−O chains only implies a slight decrease in the spread of one single WF. This *decrease* is expected to be larger than the decrease in the variance because this latter quantity is an average value over 9 WF that are not modified to the same extent during the phase transition.

2.6 Conclusions

Using a plane wave-pseudopotential approach to DFT we computed the electron localization tensor for various oxides. Our study was based on the work on semiconductors performed by Sgiarovello and co-workers but used linear-response techniques to compute the first-order wavefunctions.

In order to investigate the properties of electrons occupying individual groups of bands independently, we first set-up a band by band decomposition of the localization tensor. In analogy with the field of statistics we had to distinguish between variance and covariance in this decompositon. The significance of these new concepts was illustrated in terms of WF and explained on a simple model. The variance allows to get some insight into the hybridizations of atomic orbitals. The covariance can be useful to help constructing maximally localized WF: It identifies the bands that have to be considered together in order to improve their localization. We also made a connection between the localization tensor and the Born effective charges and we discussed the difference between all-electron and pseudopotential calculations.

We applied these techniques to binary oxides (BaO and α-PbO) as well as perovskite ferroelectrics ($BaTiO_3$ and $PbTiO_3$). By considering first the electrons of the inner bands we showed that some of them present a strong delocalization with respect to the situation in an isolated atom. This observation suggests that the underlying atomic orbitals are chemically not inert but present non negligible covalent interactions. This fact had been confirmed from an inspection of the Born effective charges.

Finally, the variations of the O 2p variance during the ferroelectric phase transitions of $BaTiO_3$ were found to be very small. This surprizing result was explained in terms of

the electronic structure of this compound as it is interpreted in the Harrison model.

We think that, when combined with Born effective charges, the band-by-band decomposition of the localization tensor could provide a powerful tool for the qualitative characterization of bonds in solids. However, more studies are needed, for different classes of materials, in order to make it fully effective.

Conclusions

Using density functional theory we studied ground-state and linear response properties of $LiNbO_3$ and the localization tensor in various oxides.

In the first chapter, we investigated the dielectric and dynamical properties of $LiNbO_3$. In particular, we clarified the assignation of the zone-center optical phonons. In addition, we adressed more fundamental questions such as the origin of the giant Born effective charges in the paraelectric phase and the mechanism responsible for the phase transition. The first point has been clarified from a band-by-band decomposition. This technique revealed the particular electronic structure, especially the hybridization between O 2p and Nb 4d states, to be responsible for the anomalous values of the Born effective charges. To investigate the second point, we used a microscopic model constructed from first-principles calculations. This model allowed us to relate the structural instability to the long-range Coulomb interactions between atoms.

In the second chapter we applied the Berry phase theory of polarization to the fundamental problem of electron localization in insulating crystals. We first set up a band-by-band decomposition of the localization tensor. In the first chapter, such a decomposition allowed us to clarify the origin of the anomalous Born effective charges in $LiNbO_3$. In the case of the localization tensor it gave an even deeper insight in the electronic structure of ferroelectrics since it clarified the kind of hybridizations that take place in these compounds. We paied a particular attention to the variations of electron localization during the ferroelectric phase transition of $BaTiO_3$ and showed that the slightly stronger localization in the ferroelectric phase agrees with the electronic structure of this compound as it is interpreted in the Harisson model.

The results presented in the first and second chapter have been published recently [18, 19]. At the time being, other works are in progress. In fact, these two chapters are a first step in the study of non-linear optical properties from first-principles. For example, the quantities presented in the first chapter will be useful to compute the electrooptic tensor and the Raman scattering efficiencies in $LiNbO_3$. The details of this study will be left for a later discussion. Here, we just want to mention a few points in close relationship with the topics discussed in this work. The computation of the Raman intensities in $LiNbO_3$ confirms our assignation of the zone-center phonons in the first chapter. This gives us an other strong argument in favour of our assignation. Moreover, the computation of the electrooptic coefficients in various oxides revealed that the soft mode dominates the amplitude of these coefficients. A similar domination has been observed for the dielectric tensor of $LiNbO_3$ discussed in the first chapter. Our results underline the important role

of the soft mode in the electromechanical response of ferroelectric oxides that is exploited in many applications.

Appendix A

Optical conductivity

The optical conductivity (imaginary part of the optical dielectric tensor) of a given material is related to its absorption coefficient, the probability of the valence electrons to perform optical transitions to the *unoccupied* conduction bands under the influence of an electromagnetic field. If we consider only "vertical" band-to-band transitions (thus neglecting elementary excitations like the electron-hole interaction or the electron-phonon coupling) this quantity writes in the dipolar approximation [90]

$$\varepsilon''_{\alpha\beta}(\omega) = \frac{4\pi^2 e^2}{m^2\omega^2\hbar} \sum_{n=1}^{N} \sum_{m=N+1}^{\infty} \int_{BZ} \frac{2d\mathbf{k}}{(2\pi)^3} p^{\alpha}_{nm}(\mathbf{k}) p^{\beta}_{mn}(\mathbf{k}) \delta\left(\omega_{mn}(\mathbf{k}) - \omega\right) \tag{A.1}$$

where m is the electron mass, $\mathbf{p}_{nm}(\mathbf{k}) = -i\hbar\langle\psi_{n\mathbf{k}}|\nabla\psi_{m\mathbf{k}}\rangle$ and $\hbar\omega_{mn}(\mathbf{k}) = \varepsilon_{m\mathbf{k}} - \varepsilon_{n\mathbf{k}}$. The matrix elements of the momentum operator can equivalently be expressed as $\mathbf{p}_{nm}(\mathbf{k}) = -m\omega_{nm}(\mathbf{k})\langle u_{n\mathbf{k}}|\partial_{\mathbf{k}} u_{m\mathbf{k}}\rangle$.

It has been shown by Souza, Wilkens and Martin [77] that ε'' is related to the localization tensor by the relation

$$\int_0^{\infty} \varepsilon''_{\alpha\beta}(\omega)\, d\omega = \frac{8\pi^2 e^2 N}{\hbar V_c} \left\langle r_\alpha r_\beta \right\rangle_c . \tag{A.2}$$

In order to see the effect of the band by band decomposition, we will write ε'' as

$$\varepsilon''_{\alpha\beta}(\omega) = \sum_{i=1}^{N_g} \left\{ \varepsilon''_{\alpha\beta}(\omega; G_i) + \sum_{j\neq i}^{N_g} \varepsilon''_{\alpha\beta}(\omega; G_i, G_j) \right\} \tag{A.3}$$

where

$$\varepsilon''_{\alpha\beta}(\omega; G_i) = \frac{4\pi^2 e^2}{m^2\omega^2\hbar} \sum_{n\in G_i} \sum_{m\notin G_i}^{\infty} \int_{BZ} \frac{2d\mathbf{k}}{(2\pi)^3} p^{\alpha}_{nm}(\mathbf{k}) p^{\beta}_{mn}(\mathbf{k}) \delta\left(\omega_{mn}(\mathbf{k}) - \omega\right) \tag{A.4}$$

$$\varepsilon''_{\alpha\beta}(\omega; G_i, G_j) = \frac{-4\pi^2 e^2}{m^2\omega^2\hbar} \sum_{n\in G_i} \sum_{m\in G_j} \int_{BZ} \frac{2d\mathbf{k}}{(2\pi)^3} p^{\alpha}_{nm}(\mathbf{k}) p^{\beta}_{mn}(\mathbf{k}) \delta\left(\omega_{mn}(\mathbf{k}) - \omega\right) . \tag{A.5}$$

The first sum of Eq. (A.4) has to be taken over the bands of group G_i while the second sum extends over all bands (unoccupied or not) except those of group G_i. In Eq. (A.5),

the two sums extend over the bands of group G_i and G_j. It is easy to show that $\varepsilon''_{\alpha\beta}(\omega; G_i)$ and $\varepsilon''_{\alpha\beta}(\omega; G_i, G_j)$ are related to the variances and covariances by the relations

$$\int_0^\infty \varepsilon''_{\alpha\beta}(\omega; G_i) d\omega = \frac{8\pi^2 e^2 n_i}{\hbar V_c} \langle r_\alpha r_\beta \rangle_c (G_i) \tag{A.6}$$

$$\int_0^\infty \varepsilon''_{\alpha\beta}(\omega; G_i, G_j) d\omega = \frac{8\pi^2 e^2 n_i n_j}{\hbar V_c} \langle r_\alpha r_\beta \rangle_c (G_i, G_j). \tag{A.7}$$

Thanks to these definitions, the physical meaning of the covariance becomes now obvious: If the total localization tensor was simply the sum of the variances $\langle r_\alpha r_\beta \rangle_c (G_i)$, the expression of the dielectric tensor (A.1) would not only contain transitions between occupied and unoccupied states, but also transitions between occupied states themselves. It is by adding the covariances $\langle r_\alpha r_\beta \rangle_c (G_i, G_j)$ that one compensates the effect of these forbidden transitions in order to get a physically correct quantity.

Bibliography

[1] M. E. Lines and A. M. Glass, "Principles and applications of ferroelectrics and related materials", Clarendon Press, Oxford (1977).

[2] O. Auciello, J. F. Scott and R. Ramesh, Physics Today, 22 (July 1998).

[3] J. Junquera and Ph. Ghosez, Nature **22**, 506 (2003).

[4] H. Fu and R. E. Cohen, Nature **403**, 281 (2000);

[5] S.-E. Park and T. R. Shrout, J. Appl. Phys. **82**, 1804 (1997).

[6] H. Nishihara, M. Haruna and T. Suhara, "Optical integrated circuits", McGRAW-HILL optical and electro-optical engineering series, Edited by R. E. Fischer and W. J. Smith (1985).

[7] L. Wooten, K. M. Kissa, A. Yi-Yan, E. J. Murphy, D. A. Lafaw, P. F. Hallemeier, D. Maack, D. V. Attanasio, D. J. Fritz, G. J. McBrien and D. E. Bossi, IEEE journal of selected topics in quantum electronics **6**, 69 (2000).

[8] K. Buse, A. Adibi and D. Psalti, Nature **393**, 665 (1998).

[9] L. Hesselink, S. S. Orlov, A. Liu, A. Akella, D. Lande and R. R. Neurgaonkar, Science **282**, 1089 (1998).

[10] P. Hohenberg et W. Kohn, Phys. Rev. **136**, B864 (1964).

[11] W. Kohn et L. J. Sham, Phys. Rev. **140**, A1133 (1965).

[12] R. Resta, Modelling Simul. Mater. Sci. Eng. **11**, R69 (2003).

[13] R. Resta, Rev. Mod. Phys. **66**, 899 (1994).

[14] R. D. King-Smith and D. Vanderbilt, Phys. Rev. B **47**, 1651 (1993).

[15] D. Vanderbilt and R. D. King-Smith, Phys. Rev. B **48**, 4442 (1993).

[16] C. Sgiarovello, M. Peressi and R. Resta, Phys. Rev. B **64**, 115202 (2001).

[17] U. V. Waghmare, N. A. Spaldin, H. C. Kandpal and R. Seshadri, Phys. Rev. B **67**, 125111 (2003).

[18] M. Veithen and Ph. Ghosez, Phys. Rev. B **65**, 214302 (2002).

[19] M. Veithen, X. Gonze and Ph. Ghosez, Phys. Rev. B **66**, 235113 (2002).

[20] W. Zhong, D. Vanderbilt and K. M. Rabe, Phys. Rev. Lett **73**, 1861 (1994).

[21] A. Räuber, Current Topics in Materials Science, volume 1, edited by E. Kaldis (North-Holland Publishing Company, 1978), p. 481.

[22] I. Inbar and R. E. Cohen, Phys. Rev. B **53**, 1193 (1996).

[23] I. Inbar and R. E. Cohen, Ferroelectrics **194**, 83 (1997).

[24] A. V. Postnikov, V. Caciuc and G. Borstel, J. Phys. Chem. Solids **61**, 295 (2000).

[25] V. Caciuc, A. V. Postnikov and G. Borstel, Phys. Rev. B **61**, 8806 (2000).

[26] K. Parlinski, Z. Q. Li and Y. Kawazoe, Phys. Rev. B **61**, 272 (2000).

[27] ABINIT [X. Gonze *et al.*, Comput. Mater. Sci. **25**, 478 (2002)] is a common project of the Université Catholique de Louvain, Corning Incorporated, and other contributors (URL http://www.abinit.org). It relies on an efficient Fast Fourier Transform algorithm [28] for the conversion of wavefunctions between real and reciprocal space, on the adaptation to a fixed potential of the band-by-band conjugate gradient method [29] and on a potential-based conjugated-gradient algorithm for the determination of the self-consistent potential [30]. In addition to usual ground-state calculations it allows linear-response computations of the phonon frequencies, Born effective charges and dielectric constants [31, 32].

[28] S. Goedecker, newblock SIAM J. on Scientific Computing **18**, 1605 (1997).

[29] M. C. Payne, M. P. Teter, D. C. Allan, T. A. Arias et J. D. Joannopoulos, Rev. Mod. Phys **64**, 1045 (1992).

[30] X. Gonze, Phys. Rev. B **54**, 4383 (1996).

[31] X. Gonze and C. Lee, Phys. Rev. B **55**, 10355 (1997).

[32] X. Gonze, Phys. Rev. B **55**, 10337 (1997).

[33] J. P. Perdew and Y. Wang, Phys. Rev. B **45**, 13244 (1992).

[34] J. P. Perdew, K. Burke and M. Ernzerhof, Phys. Rev. Lett. **77**, 3865 (1996).

[35] N. Troullier and J. L. Martins, Phys. Rev. B **43**, 1993 (1991).

[36] M. Fuchs and M. Scheffler, Comuter Physics Communications **119**, 67 (1999).

[37] H. J. Monkhorst and J. D. Pack, Phys. Rev. B **13**, 5188 (1976).

[38] H. Boysen and F. Altorfer, Acta Cryst. **B 50**, 405 (1994).

[39] J. Goniakowski, J. M. Holender, L. N. Kantorovich and M. J. Gillan, Phys. Rev. B **53**, 957 (1996).

[40] C. Filippi, D. J. Singh and C. J. Umrigar, Phys. Rev. B **50**, 14947 (1994).

[41] G. F. Koster, Solid State Physics, edited by F. Seitz and D. Turnball (Academic, New York, 1957), p. 173.

[42] Ph. Ghosez, X.Gonze and J.-P. Michenaud, Ferroelectrics **220**, 1 (1999).

[43] R. D. King-Smith and D. Vanderbilt, Phys. Rev. B **49**, 5828 (1994).

[44] R. E. Cohen, Nature **358**, 136 (1992).

[45] R. E. Cohen and H. Krakauer, Ferroelectrics **136**, 65 (1992).

[46] R. O. Jones and O. Gunnarson, Rev. Mod. Phys. **61**, 689 (1989).

[47] A. Dhar and A. Mansingh, J.Appl.Phys. **68**, 5804 (1990).

[48] S. H. Wemple, M. DiDomenico Jr. and I. Camlibel, Appl. Phys. Lett. **12**, 209 (1968).

[49] A. M. Glass and M. E. Lines, Phys. Rev. B **13**, 180 (1976).

[50] L. Hafid and F. M. Michel-Calendini, J. Phys. C: Sol. State Phys. **19**, 2907 (1986).

[51] W. Zhong, R. D. King-Smith and D. Vanderbilt, Phys. Rev. Lett. **72**, 3618 (1994).

[52] X. Gonze, Ph. Ghosez and R. W. Godby, Phys. Rev. Lett. **78**, 294 (1997).

[53] The overestimate (10%) is smaller than that usually observed for perovskite ABO_3 compounds (20%). This can be related to the smaller discrepancy obtained for the electronic bandgap in the case of $LiNbO_3$.

[54] X. Gonze, Ph. Ghosez and R. W. Godby, Phys. Rev. Lett. **74**, 4035 (1995).

[55] Ph. Ghosez, X. Gonze and R. W. Godby, Phys. Rev. B **56**, 12811 (1997).

[56] Ph. Ghosez, X. Gonze and J.-P. Michenaud, Europhys. Lett. **33**, 713 (1996).

[57] C. Z. Wang, R. Yu and H. Krakauer, Phys. Rev. B **54**, 11161 (1996).

[58] Ph. Ghosez, J.-P. Michenaud et X. Gonze, Phys. Rev. B **58**, 6224 (1998).

[59] Harrison W. A., "Electronic structure and the properties of solids", W. H. Freeman and Co, San Fransisco, 1980.

[60] W. Cochran, Adv. Phys. **9**, 387 (1960).

[61] X. Gonze, J. C. Charlier, D. C. Allan and M. P. Teter, Phys. Rev. B **50**, 13035 (1994).

[62] A. Ridah, M. D. Fontana and P. Bourson, Phys. Rev. B **56**, 5967 (1997).

[63] A. Ridah, P. Bourson, M. D. Fontana and G. Malovichko, J. Phys.: Condens. Matter **9**, 9687 (1997).

[64] U. T. Schwarz and M. Maier, Phys. Rev. B **55**, 11041 (1997).

[65] A. S. Barker Jr. and R. Loudon, Phys. Rev. **158**, 433 (1967).

[66] M. R. Chowdhury, G. E. Peckham and D. H. Saunderson, J.Phys.C: Solid State Phys **11**, 1671 (1978).

[67] Y. Repelin, E. Husson, F. Bennani and C. Proust, J. Phys. Chem. Solids **60**, 819 (1999).

[68] I. P. Kaminow and W. D. Johnston Jr, Phys. Rev. **160**, 519 (1967).

[69] R. Claus, G. Borstel, E. Wiesendanger and L. Steffan, Z. Naturforsch. A **27A**, 1187 (1972).

[70] X. Yang, G. Lan, B. Li and H. Wang, Phys. stat. sol. (b) **142**, 287 (1987).

[71] W. Kohn, Phys. Rev. **133**, A171 (1964).

[72] G. Ortiz and R. M. Martin, Phys. Rev. B **49**, 14202 (1994).

[73] R. Resta, Phys. Rev. Lett. **80**, 1800 (1998).

[74] R. Resta and S. Sorella, Phys. Rev. Lett. **82**, 370 (1999).

[75] A. A. Aligia and G. Ortiz, Phys. Rev. Lett. **82**, 2560 (1999).

[76] R. Resta, J. Phys.: Condens. Matter **14**, R625 (2002).

[77] I. Souza, T. Wilkens and R. M. Martin, Phys. Rev. B **62**, 1666 (2000).

[78] N. Marzari and D. Vanderbilt Phys. Rev. B **56**, 12847 (1997).

[79] N. Marzari and D. Vanderbilt, in *First-Principles Calculations for Ferroelectrics*, edited by R. E. Cohen, AIP Conf. Proc. No. 436 (AIP, Woodbury, 1998), p. 146.

[80] M. Posternack, A. Baldereschi, H. Krakauer and R. Resta, Phys. Rev. B **55**, 15983 (1997).

[81] Ph. Ghosez, X. Gonze, Ph. Lambin and J.-P. Michenaud, Phys. Rev. B **51**, 6765 (1995).

[82] Ph. Ghosez and X. Gonze, J. Phys.: Condens. Matter **12**, 9179 (2000).

[83] X. Gonze, Phys. Rev. A **52**, 1096 (1995).

[84] M. P. Teter, Phys. Rev. B **48**, 5031 (1993).

[85] Ph. Ghosez, X. Gonze and J.-P. Michenaud, Ferroelectrics **220**, 1 (1999).

[86] P. Pertosa and F. M. Michel-Calendini, Phys. Rev. B **17**, 2011 (1978).

[87] G. W. Watson, S. C. Parker and G. Kresse, Phys. Rev. B **59**, 8484 (1999).

[88] C. B. Van de Walle and P. E. Blöchl, Phys. Rev. B **47**, 4244 (1993).

[89] M. Veithen, X. Gonze and Ph. Ghosez, to appear in *Fundamental Physics of Ferroelectrics*, edited by R. E. Cohen, AIP Conf. Proc. (Washington 2002).

[90] F. Bassani and G. Pastori Parravicini, *Electronic States and Optical Transitions in Solids* (Pergamon, Oxford, 1975).